A stable atmospheric-pressure plasma for extreme-temperature synthesis

https://doi.org/10.1038/s41586-023-06694-1

Received: 10 January 2023

Accepted: 28 September 2023

Published online: 29 November 2023

Check for updates

Hua Xie[1,10], Ning Liu[2,10], Qian Zhang[1,10], Hongtao Zhong[2], Liqun Guo[3], Xinpeng Zhao[1], Daozheng Li[4], Shufeng Liu[1], Zhennan Huang[1], Aditya Dilip Lele[2], Alexandra H. Brozena[1], Xizheng Wang[1], Keqi Song[5], Sophia Chen[2], Yan Yao[3], Miaofang Chi[6], Wei Xiong[4], Jiancun Rao[7], Minhua Zhao[1], Mikhail N. Shneider[2], Jian Luo[5], Ji-Cheng Zhao[1]✉, Yiguang Ju[2,8]✉ & Liangbing Hu[1,9]✉

Plasmas can generate ultra-high-temperature reactive environments that can be used for the synthesis and processing of a wide range of materials[1,2]. However, the limited volume, instability and non-uniformity of plasmas have made it challenging to scalably manufacture bulk, high-temperature materials[3–8]. Here we present a plasma set-up consisting of a pair of carbon-fibre-tip-enhanced electrodes that enable the generation of a uniform, ultra-high temperature and stable plasma (up to 8,000 K) at atmospheric pressure using a combination of vertically oriented long and short carbon fibres. The long carbon fibres initiate the plasma by micro-spark discharge at a low breakdown voltage, whereas the short carbon fibres coalesce the discharge into a volumetric and stable ultra-high-temperature plasma. As a proof of concept, we used this process to synthesize various extreme materials in seconds, including ultra-high-temperature ceramics (for example, hafnium carbonitride) and refractory metal alloys. Moreover, the carbon-fibre electrodes are highly flexible and can be shaped for various syntheses. This simple and practical plasma technology may help overcome the challenges in high-temperature synthesis and enable large-scale electrified plasma manufacturing powered by renewable electricity.

Plasma creates highly reactive and non-equilibrium environments that are used in various materials syntheses and processes[1,2,9,10]. However, the fabrication of large-scale, particularly high-melting point, bulk materials requires a plasma discharge process that can achieve uniform high temperatures over a large area or volume. Volumetric plasmas, such as glow discharge, have been previously demonstrated through a variety of methods, although typically at low pressure[11] (<150 torr) at which the neutral gas temperature (T_g) of the plasma is much lower[3–6] (<1,000 K) than the electron temperature (T_e) (refs. 4,12,13). As a result, glow discharge has a very limited ability to process high-temperature materials at a high yield. Alternatively, arc discharge is often used to achieve high-temperature plasmas (up to 10,000 K or higher) and enable atmospheric pressure manufacturing[14–18]. However, atmospheric arc discharge between conventional plate electrodes typically contracts to a narrow, random arc channel (about 1 mm), with the resulting temperature distribution being highly non-uniform because of energy dissipation to the surrounding environment[7,8]. As a result, arc discharge has a limited ability to process large-scale materials, particularly those with planar form factors.

Various electrode designs and processes have been explored to improve the stability and scale of high-temperature plasma discharge at atmospheric pressure. For example, pin-to-pin electrodes can prevent random plasma discharge, in which the high curvature of the electrodes (radius of several millimetres) increases the local electric field strength and promotes the thermionic emission of secondary electrons to achieve stable high-temperature plasmas. However, the pin structure limits the arc plasmas to a narrow channel[19], with a limited plasma volume. Although a rotating gliding arc can increase the discharge volume[20], the plasma channel is still a filament, with a non-uniform distribution of the temperature and active species. Thus, to our knowledge, the challenge of atmospheric-pressure, high-temperature plasma synthesis and processing remains to be addressed for the scalable manufacturing of high-temperature, bulk materials.

Here we report a uniform, ultra-high temperature (up to 8,000 K), stable plasma (USP) at atmospheric pressure that is achieved using a pair of carbon-tip-enhanced electrodes (Fig. 1a,b and Extended Data Fig. 1a,b). The electrodes are composed of a high density (around 10^5 cm^{-2}) of short, vertically oriented carbon fibres (approximately 10 μm diameter; Extended Data Fig. 1c–f), as well as some long carbon fibres that extend into the gap between the two electrodes and form contact (Extended Data Fig. 1d). When voltage is applied, Joule heating is intensified at the defective regions or contact points of the

[1]Department of Materials Science and Engineering, University of Maryland, College Park, MD, USA. [2]Department of Mechanical and Aerospace Engineering, Princeton University, Princeton, NJ, USA. [3]Department of Electrical and Computer Engineering and Texas Center for Superconductivity at the University of Houston (TcSUH), University of Houston, Houston, TX, USA. [4]Department of Mechanical Engineering and Materials Science, University of Pittsburgh, Pittsburgh, PA, USA. [5]Department of NanoEngineering, University of California San Diego, La Jolla, CA, USA. [6]Center for Nanophase Materials Sciences, Oak Ridge National Laboratory, Oak Ridge, TN, USA. [7]Advanced Imaging and Microscopy Laboratory, University of Maryland, College Park, MD, USA. [8]Princeton Plasma Physics Laboratory, Princeton, NJ, USA. [9]Center for Materials Innovation, University of Maryland, College Park, MD, USA. [10]These authors contributed equally: Hua Xie, Ning Liu, Qian Zhang. ✉e-mail: jczhao@umd.edu; yju@princeton.edu; binghu@umd.edu

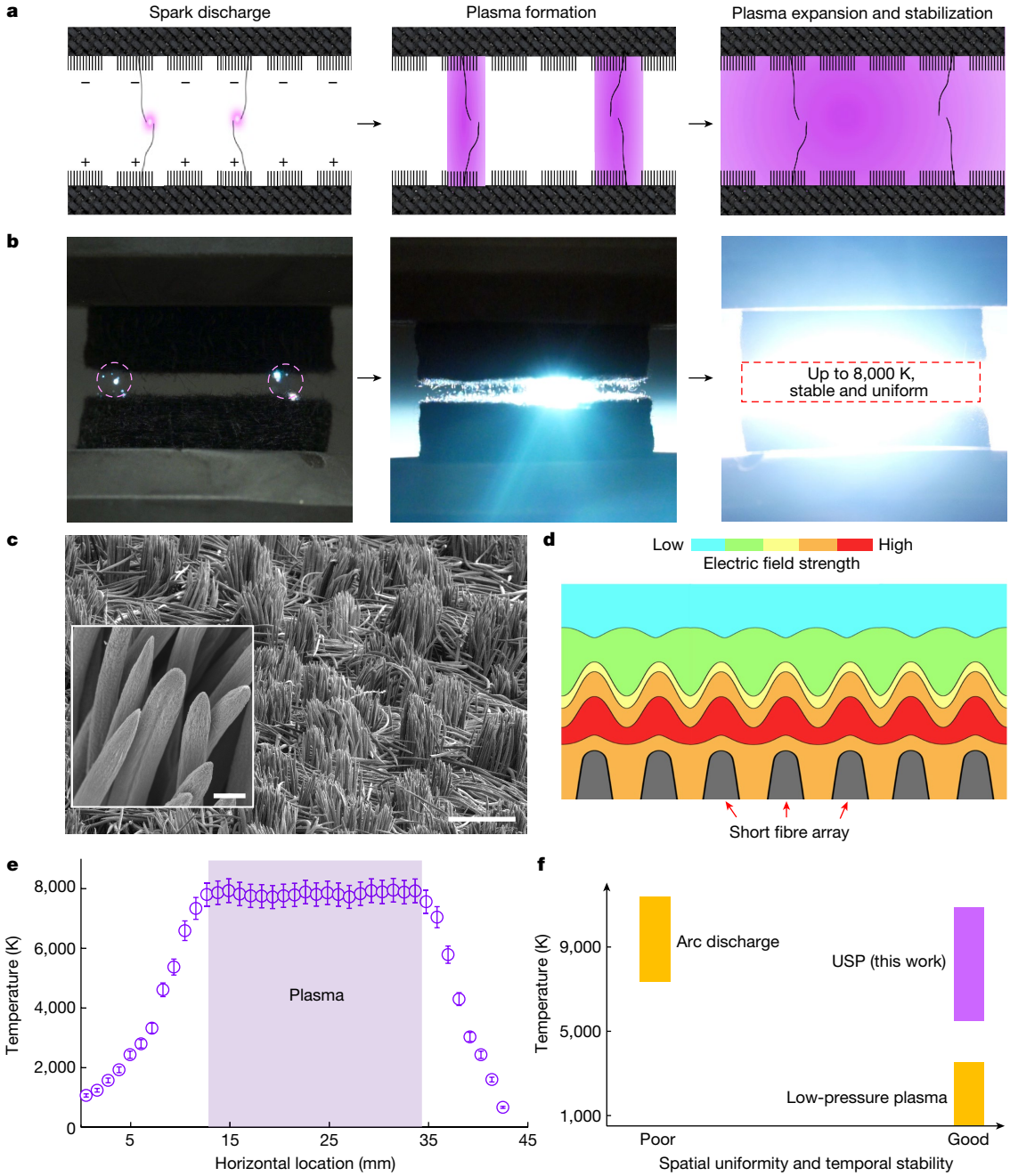

Fig. 1 | A uniform USP at atmospheric pressure enabled by an electrode design featuring long carbon fibres and a densely spaced array of numerous, small-diameter carbon-fibre tips. a,**b**, Schematic (**a**) and corresponding photographs (**b**) of the volumetric plasma generation using the carbon-fibre-tip electrodes. **c**, SEM image of the short-fibre-tip array on the surface of the carbon felt electrode. Scale bar, 200 µm. Inset, magnified image showing the fibres. Scale bar, 10 µm. **d**, Schematic of the short carbon fibres, showing the tip-enhanced electric field distribution when the plasma discharge breakdown takes place, in which the carbon-tip array coalesces and strengthens the local electric field intensity across the electrode surface. **e**, The temperature profile of the plasma along the carbon felt electrodes, which can reach temperatures as high as about 8,000 K with excellent spatial uniformity. Error bars show s.d.; $n = 50$. **f**, Temperature and uniformity comparison of USP with other plasma techniques using similar levels of current input[22–27], showing the advantage of USP in generating a steady, large-area atmospheric plasma with high temperatures (up to about 8,000 K).

long carbon fibres, at which the resistance is the highest, reaching an ultra-high temperature until the fibres break (Extended Data Fig. 2a–c), creating very small gaps (about 10 µm). The locally enhanced electric fields at these newly formed fibre tips promote secondary electron emission, resulting in a spark discharge across the narrow inter-fibre gaps[21] (Fig. 1b and Extended Data Fig. 2a) that helps in initiating the plasma at a record-low breakdown voltage (around 40–45 V). Meanwhile, the densely spaced short carbon fibres, as shown in the scanning electron microscopy (SEM) image of Fig. 1c, produce tip-enhanced electric fields that merge across the surface of the electrodes (Fig. 1d), accelerating the Townsend breakdown to arc transition, expanding the plasma size and volume and increasing the plasma uniformity (Extended Data Fig. 2a). This expansion also generates a collective heating effect that helps stabilize the plasma.

With this technique, we can readily achieve a continuous, volumetric plasma (dictated by the size of the electrodes) featuring a highly controllable temperature of between 3,000 K and 8,000 K, as well as a uniform temperature distribution (Fig. 1e). Compared with other

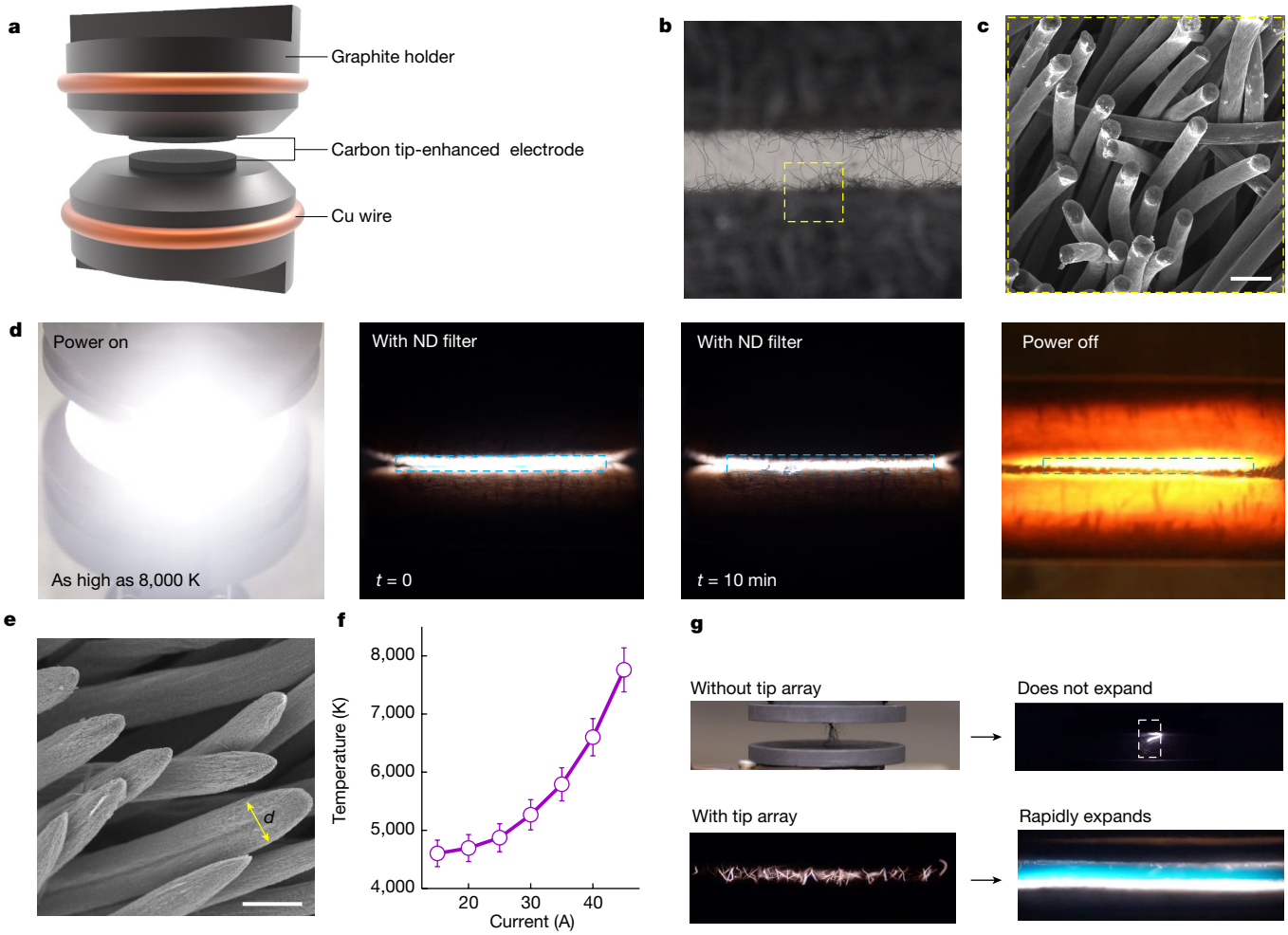

Fig. 2 | USP plasma generation using the carbon-tip-enhanced electrode design. a, Schematic of the set-up used for the USP process. The electrodes are composed of 25.4-mm round discs of carbon felt embedded in graphite bases. The carbon felt has both short and long vertically oriented carbon fibres on each electrode surface. **b**, Magnified photograph of the two electrodes, in which the sparser, long fibres from the two electrodes form initial contacts. **c**, SEM image of the short, higher-density, vertical carbon-fibre bundles. These carbon fibres initially featured blunt tips. **d**, Applying a voltage between the electrodes results in gas discharge, with the plasma displaying an extremely bright light. To view the plasma more clearly, we applied a neutral density (ND) filter, which demonstrated the uniformity of the plasma between the electrodes. The plasma showed good stability when the voltage was applied, shown here for 10 min. Turning off the input voltage then caused the plasma to stop, although the carbon felt electrode remained red-hot immediately after the plasma termination. **e**, SEM images of the short carbon fibres immediately after the plasma formation, showing the fibre tips have become sharper. **f**, The temperature of the central region of the plasma as a function of the input current (15–45 A, corresponding to a current density change of 3–9 A cm^{-2}). Error bars show s.d.; $n = 50$. **g**, Experimental comparison of the plasma formation process between the graphite plate electrodes with only long fibres (that is, without the short-fibre-tip array) (top) and the carbon-tip-enhanced electrodes with both long fibres and the short-fibre-tip array (bottom). The short fibres are necessary for the electrodes to expand and stabilize the plasma. Scale bars, 20 μm (**c**); 10 μm (**e**).

arc jet or pin-to-pin arc plasmas[22–27] (Fig. 1f), the USP process can achieve a uniformly large area and high temperature (for example, 8,000 K) at atmospheric pressure with modest current input (about 45 A). Notably, the carbon-fibre tips remain stable even under these ultra-high-temperature conditions because of the low heat capacity as well as the high thermal conductivity and emissivity of the carbon electrodes. As a result, the volumetric plasma can maintain stable operation for 10 min or longer with sustained power input.

As a proof of concept, we used this USP technique to synthesize several extreme materials in just seconds, including hafnium carbonitride (Hf(C,N), an ultra-high-temperature ceramic), refractory metal alloys with ultra-high melting points (for example, a W–1.5Nb–0.5Ti alloy) and carbon nanotubes (CNTs) directly from carbon black without any catalyst. The plasma temperature can also be rapidly tuned and pulsed (with heating and cooling rates of around 10^3 K s^{-1}), which can be used for various non-equilibrium syntheses[28,29]. Furthermore, the carbon-fibre electrodes are highly flexible and can be shaped into different configurations, such as a plasma heating channel or a scanning beam, to enable the processing of a wide range of materials. This continuous and volumetric plasma overcomes the traditional trade-off of plasma size, temperature and uniformity using a simple, carbon-fibre-tip electrode design, suggesting its potential for large-scale, sustainable manufacturing of high-temperature materials[30].

Figure 2a shows a schematic of the electrode set-up used to generate the USP process at atmospheric pressure. Two disc electrodes are made of carbon felt (25.4 mm diameter; Extended Data Fig. 1a,b). We then vertically aligned two of these carbon felt electrodes (Fig. 2a, Extended Data Fig. 2a) separated by a gap of about 3 mm in an argon environment at atmospheric pressure. In this set-up, several long carbon fibres extend from the carbon felt surfaces and form contacts between the two electrodes (Fig. 2b). Furthermore, the electrode surface features a high density of short, vertically oriented carbon fibres with blunt tips that are separated by horizontally aligned fibres, with an inter-bundle distance of about 200 μm (Extended Data Fig. 1c). The carbon-fibre

tips feature diameters of approximately 10 μm (Fig. 2c), which is much smaller than the micron-to-centimetre scale of the metal pin electrodes conventionally used for generating arc plasmas[31–33].

To start the USP process, we gradually increased the voltage between the electrodes (up to around 33 V). The long fibres that contact each other generate strong Joule heating, which causes the fibres to glow (Extended Data Fig. 2a and Supplementary Video 1). Note that the defective regions and contact points between the long fibres have a higher resistance than that of the fibres themselves, which leads to localized heating and breakage, forming small gaps between the fibres (Extended Data Fig. 3). This process creates an open-circuit condition, which causes the fibres that were glowing previously to turn dark (Extended Data Fig. 2). However, as we continue to increase the voltage, these new micron-sized gaps between the fibres pronouncedly reduce the gas breakdown voltage (about 42 V) and increase the ability to discharge using the enhanced electric field and increased secondary electron emission at the fibre tips, with sparks forming between the long fibre tips and initiating the plasma. The gas discharge then rapidly coalesces between the electrodes, which we consider was because of the presence of the short carbon-fibre tips that cover the surface.

The resulting USP plasma generates an extremely bright light, in which a neutral density filter is required to observe the plasma (Fig. 2d). The plasma remains stable, in this case lasting for at least 10 min until we turned the power supply off (Fig. 2d, Extended Data Fig. 4a and Supplementary Video 2). We found that the carbon-fibre tips were sharpened by the plasma generation process (Fig. 2e and Extended Data Fig. 4b), probably because of the concentrated electric fields. The sharp tips should also further increase the surrounding local electric field and facilitate the discharge process. Our modelling suggests that this localized tip-enhanced electric field merges across the surface of the electrodes because of the high-density array of the short carbon fibres, resulting in the observed volumetric, stable plasma formation (Extended Data Fig. 4c).

We determined the USP temperature using Rayleigh thermometry[34,35]. As shown in Fig. 2f, when we increased the current from 15 A to 45 A (corresponding to a current density of 3–9 A cm^{-2}), the plasma temperature increased from about 4,600 K to 7,700 K, demonstrating the ability of the USP process to generate an ultra-high-temperature environment, which we further confirmed using grey-body radiation spectroscopy (Extended Data Fig. 5a). We also found that the temperature shows good uniformity across the centre of the plasma (Extended Data Fig. 5b). Despite such an ultra-high plasma temperature, numerical simulation shows that the carbon tips feature a lower temperature distribution, reaching just around 3,000 K even when the plasma centre is set at 7,000 K (Extended Data Fig. 5c). We attribute this to the high thermal conductivity and emissivity of the carbon tips, which helps rapidly transfer heat away from the electrodes. This explains how the carbon tips remain stable in such an ultra-high-temperature environment that is essential for the continuous operation of the plasma.

We conducted several control experiments to better understand the role of the short and long carbon fibres in the USP process. First, using stainless-steel plate electrodes without any fibres (Extended Data Fig. 6a), we found that a voltage of almost 1,500 V was required over an approximately 3-mm gap to achieve the gas discharge breakdown, with the resulting plasma discharge occurring at random in narrow channels. Notably, the voltage is more than 30 times higher than the 42 V required using the carbon-fibre-tip-enhanced electrodes over the same electrode gap distance. We also performed control experiments isolating the effects of the long and short carbon fibres. We found that by simply removing the long fibres between the carbon felt electrodes and ensuring no contact was formed, we were unable to generate plasma breakdown under the same conditions (Extended Data Fig. 6b), demonstrating the necessity of the long carbon fibres in initiating the USP process. As an extra control experiment, we used two graphite plate electrodes of the same dimensions but with only a bundle of long fibres glued between the electrodes (that is, without the presence of the short fibre-tip array; Fig. 2g and Extended Data Fig. 6c–e). As we elevated the voltage, only spark discharge was observed, without the formation of a continuous or expanded plasma. By contrast, the USP process produces a steady volumetric plasma, which we attribute to the presence of the dense, short carbon fibres, the average distance between which (about 3–10 μm) is close to the Debye length of the system (Methods), thus enabling numerous localized tip-enhanced electric fields to coalesce across the electrodes and expand the plasma after initiation. Moreover, the high temperature of the fibre tips may enhance the secondary electron emission, which would further promote plasma expansion with enhanced uniformity using a collective heating effect.

Figure 3a presents the current–voltage (I–V) characteristics of the USP discharge process using the tip-enhanced carbon felt electrodes, with corresponding images at different stages shown in Fig. 3b. We also simultaneously measured the plasma electric field strength between the electrodes using the in situ electric-field-induced second harmonics (E-FISH) method[36] (Fig. 3c). As the top carbon felt bias voltage was increased from 0 V to about 33 V (Fig. 3a, I), we observed bright filaments between the electrodes (Fig. 3b, I), which are the Joule-heated long, contacted carbon fibres. Then from about 33–42 V, we observed no current signal in the I–V curve (Fig. 3a, II) and no light emission from the fibres (Fig. 3b, II). This outcome is because of the physical breakage of the contacted long fibres because of excessive Joule heating, forming micro-gaps between these fibres and cutting off the current (Fig. 3b, II). As we further increased the voltage to around 42–45 V (Fig. 3a, III), the electric field is further elevated (Fig. 3c) and we observed micro-spark discharges (Fig. 3b, III). These discharges occur in the narrow gaps of the broken fibres using the tip-enhanced electric field[21]. This process helps reduce the breakdown voltage of USP by promoting electron impact ionization using the Townsend avalanche[37] (Fig. 3b, IV). With the transition of micro-sparks to arc discharge, we observed a rapid drop of the voltage to about 20 V because of the increase of the electron number density and conductivity in the plasma[14,38,39] (Fig. 3a,c), with a current surge to 18 A (that is, the arc discharge breakdown current; Fig. 3a). After the breakdown, the measured electric field between the two electrodes was very low (around 5 V mm^{-1}), indicating a thermal plasma. The arc discharge volume then began to rapidly expand between the electrodes (Fig. 3b, V). When the current reached approximately 45 A (Fig. 3a,b, after VI), the USP generated a temperature of about 7,700 K (Fig. 2f). As we then gradually reduced the current from 45 A (Fig. 3a,b, VII), the arc discharge remained stable even when the current was about 7 A, which is far below the gas discharge breakdown current (around 18 A; Fig. 3a). This is a typical hysteresis of an arc plasma discharge. In general, we found that the breakdown voltage of the USP process was significantly lower than the previously reported plasma breakdown values[40,41], as well as highly reproducible (about 42 ± 2.6 V, based on 15 experiments; Extended Data Fig. 7).

We also found the volumetric plasma can be rapidly turned on and off by simply modulating the voltage and current applied. For example, we used the programmable power supply to realize a pulsed plasma by repeatedly setting the applied voltage to 45 V for 0.5 s and then turning it back to 0 V for 0.5 s (Fig. 3d and Supplementary Video 3). This process increased the current of the plasma to 35 A for 1 s. As a result, we were able to cycle the plasma temperature between 1,000 K and 6,000 K in less than 1 s, with ramping and cooling rates of about 10^3 K s^{-1}. This marked tunability is because of the low voltage barrier for the arc plasma transition enabled by the tip-enhanced electrodes. This ability to pulse the plasma to reach high temperatures for short periods of time and then quench back to low temperatures suggests that USP could be used to control reaction pathways for various non-equilibrium syntheses in which drastic temperature changes are needed (for example, rapid cooling)[28,42,43].

This continuous, volumetric, uniform and stable ultra-high-temperature plasma can be used for the synthesis of various high-temperature materials. For example, we used USP to synthesize and sinter Hf(C,N) (Fig. 4a,b), an ultra-high-temperature ceramic that is very challenging to prepare because of its record high melting point[44,45]

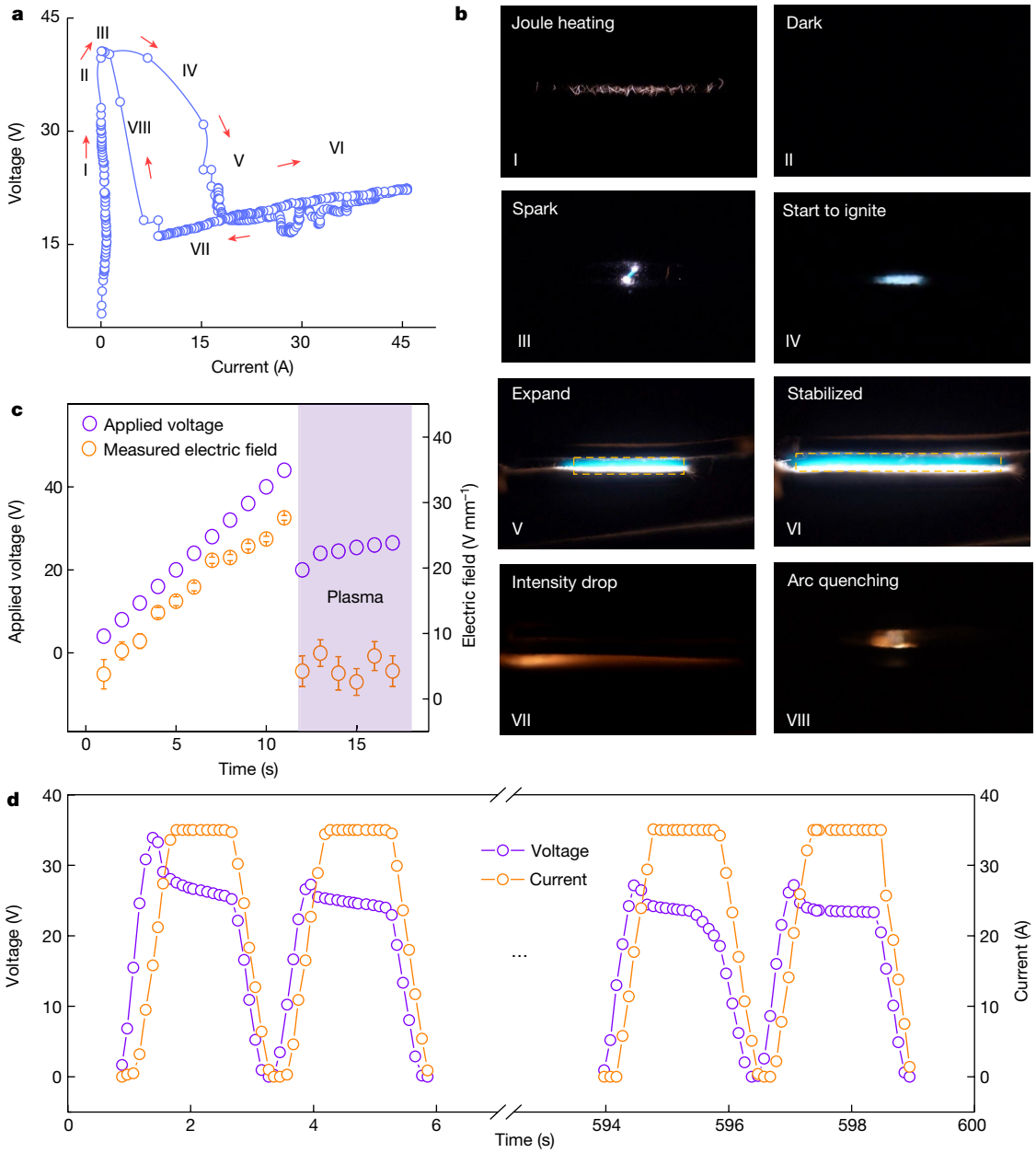

Fig. 3 | USP characterization. a,**b**, Current–voltage characteristics (**a**) and corresponding photos of the USP process at different stages (**b**). The dashed box in **b** indicates the uniform region of the plasma after formation. **c**, Measurement of the electric field between the carbon felt electrodes using the E-FISH technique. The purple data points are the applied voltage, and the orange data points with error bars correspond to the electric field between the electrodes, as measured using the E-FISH method. Error bars show s.d.; $n = 300$. **d**, The plasma can be pulsed, shown here by setting the applied voltage to 45 V for 0.5 s, then turning it off for 0.5 s, raising the current to 35 A and cycling the temperature between about 1,000 K and 6,000 K. These results suggest the potential of USP for various non-equilibrium syntheses.

(>4,000 K). The cross-sectional SEM images of the HfC/HfN pellet before (Fig. 4c) and after (Fig. 4d) the USP treatment (5,150 K for 10 s) demonstrated the successful sintering of the powder precursor mixture. After the USP heating, X-ray diffraction (XRD) confirmed that a predominantly Hf(C,N) single phase of the rock salt crystal structure (space group: $Fm\bar{3}m$) was successfully achieved[45,46] (Fig. 4e). We also used USP to synthesize a tungsten-based refractory alloy directly from metallic elemental powders (for example, W–1.5Nb–0.5Ti) to form a dense alloy with more uniform distribution of the elements (Extended Data Fig. 8a) than the compositional inhomogeneity observed when using conventional arc melting (Extended Data Fig. 8b,c). USP can also generate high-value carbon materials, such as CNTs, simply by heating carbon black without any catalysts (Extended Data Fig. 8d,e).

The fast-quenching abilities of USP, in which the temperature can drop from 6,000 K to 1,000 K in less than 1 s (Fig. 3d), can be used to synthesize high-melting-point amorphous (glassy) materials. As a demonstration, we applied USP heating and quenching to crystalline magnesium oxide (MgO), in which the fast cooling helped to maintain the spherical shape produced by surface tension in its formerly molten state (Fig. 4f). XRD of the resulting MgO shows no sharp peaks, indicating the formation of the amorphous phase (Fig. 4g) with no obvious grain boundaries in the cross-sectional SEM image (Fig. 4h).

In addition to being a facile method of generating a stable, large-area plasma, the USP process is also scalable and adaptable to different manufacturing needs. For example, we can fabricate larger carbon felt electrodes and increase the gap distance, which would allow bigger

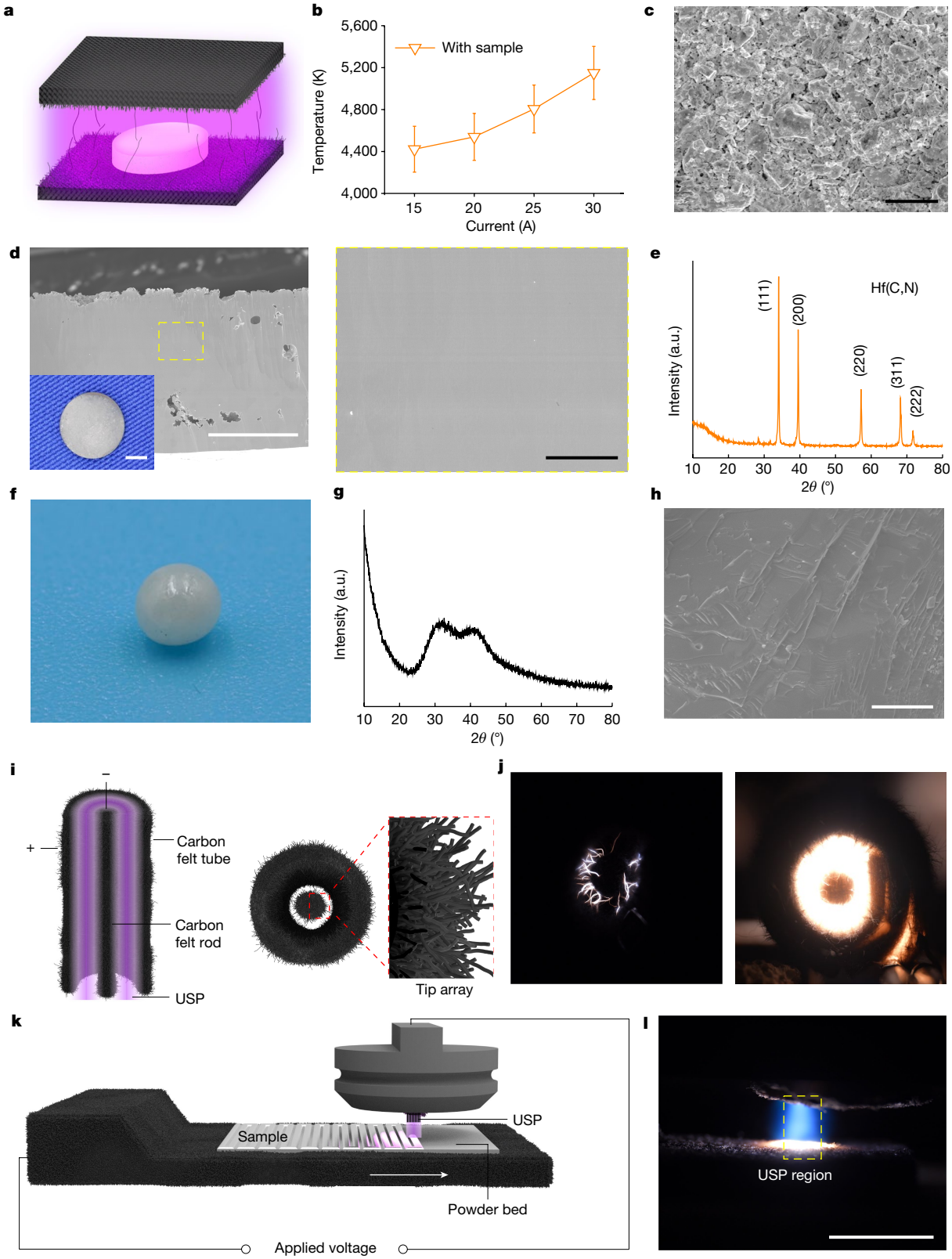

Fig. 4 | Application of USP for the synthesis of various high-temperature materials. a, Schematic demonstrating the use of USP to synthesize and sinter a ceramic pellet. **b**, The temperature of the plasma centre with the HfC/HfN pellet at an input current of 15–30 A, which is consistent with the plasma temperature without the presence of samples (Fig. 2f). Error bars show s.d.; $n = 50$. **c**, Cross-sectional SEM image of the HfC/HfN precursor pellet before sintering. Scale bar, 5 µm. **d**, Cross-sectional SEM image of the resulting Hf(C,N) after USP sintering. Scale bar, 300 µm. Inset, Hf(C,N) pellet after plasma sintering. Scale bar: 5 mm (inset); 50 µm (right). **e**, XRD pattern of the synthesized Hf(C,N). **f**, Photo of the amorphous MgO synthesized from its crystalline powder using USP rapid heating and quenching. **g**, XRD pattern of the MgO achieved using the USP method. **h**, Cross-sectional SEM image of the amorphous MgO phase showing no obvious grain boundaries. Scale bar, 20 µm. **i**,**j**, Schematic of a coaxial carbon felt rod-tube USP set-up (**i**), which can be used to form a long, volumetric plasma channel (**j**). **k**, Schematic of a focused USP beam that can be used in a powder bed fusion–sintering process. **l**, The plasma beam can be focused into a filament with a column radius of about 1 mm. Scale bar, 5 mm. a.u., arbitrary units.

samples to be processed (Extended Data Fig. 9a–c). We can also adjust the carbon felt electrode design to achieve a plasma heating channel simply by placing a carbon felt rod within a carbon felt tube to form a coaxial structure (Fig. 4i and Extended Data Fig. 9d). This design constrains the resulting plasma inside the carbon tube, forming a long, volumetric plasma channel (Fig. 4j). Because of the relatively closed environment, these USP configurations could be used for gas phase reactions, alloying refractory materials, various atomization processes and beyond. Moreover, the USP set-up can be adapted to focus the plasma into a very small region, forming a sharp front (Fig. 4k). This USP configuration could be used to increase the machining precision of the plasma for applications such as additive manufacturing (3D printing), especially powder bed fusion–sintering (Fig. 4l and Extended Data Fig. 10a–c) and coating deposition (Extended Data Fig. 10d).

Conclusion

In summary, we report a tip-enhanced carbon electrode design that enables the formation of uniform, large-area, volumetric plasma at atmospheric pressure with a record-low breakdown voltage while simultaneously achieving ultra-high temperatures of up to 8,000 K, thus overcoming the typical spatial non-uniformity and/or instability as well as the limited temperature range of conventional atmospheric plasmas. Carbon is particularly well-suited as an electrode material for plasma generation as it is highly electrically conductive, can tolerate much higher temperatures than various metals and can be cost-effectively manufactured with different fibre structures to achieve the tip-enhanced electric field effect. Furthermore, the USP set-up requires only very low electric current and voltage (<50 A and <50 V in our experiments), without the need for expensive high-power supplies and controls that are required in conventional arc-melting systems. As a result of its low cost and ease of setting up, USP enables laboratories around the world to synthesize extreme materials that can now be made using only highly specialized facilities, or not at all. We can also rapidly turn the USP process on and off, cycling the temperature between low (for example, 1,000 K) and high (for example, 6,000 K) levels in less than 1 s. This tunability enables non-equilibrium syntheses, in which controlling reaction products or phases is achieved by rapidly decreasing the temperature to avoid unwanted reaction progress.

We have demonstrated the universality of USP in the synthesis of ceramics, alloys and CNTs. Compared with other plasma techniques for materials synthesis and manufacturing (for example, arc melting), this carbon-tip-enhanced plasma offers various advantages, including a large and uniform heating area, enabling the synthesis of larger-scale materials. The flexibility of the USP electrodes also enables their adaption to different synthesis and manufacturing applications.

We expect that this technique could help address a range of challenges in high-temperature synthesis as well as promote materials discovery in the reactive plasma environment. Finally, we note that this high-temperature volumetric plasma technique can be powered using renewable electricity, suggesting its potential for large-scale green manufacturing of a wide variety of materials, including those that can withstand extreme environments (for example, ultra-high temperature, pressure and corrosion). As a result, USP could provide a platform for the synthesis of sustainable materials with widespread future applications.

Online content

Any methods, additional references, Nature Portfolio reporting summaries, source data, extended data, supplementary information, acknowledgements, peer review information; details of author contributions and competing interests; and statements of data and code availability are available at https://doi.org/10.1038/s41586-023-06694-1.

1. Merche, D., Vandencasteele, N. & Reniers, F. Atmospheric plasmas for thin film deposition: a critical review. *Thin Solid Films* **520**, 4219–4236 (2012).
2. Massines, F., Sarra-Bournet, C., Fanelli, F., Naudé, N. & Gherardi, N. Atmospheric pressure low temperature direct plasma technology: status and challenges for thin film deposition. *Plasma Process. Polym.* **9**, 1041–1073 (2012).
3. Velikhov, E. P., Golubev, V. S. & Pashkin, S. V. Glow discharge in a gas flow. *Sov. Phys. Usp.* **25**, 340–358 (1982).
4. Allis, W. P. Review of glow discharge instabilities. *Physica B+C* **82**, 43–51 (1976).
5. Nozaki, T., Yoshida, S., Karatsu, T. & Okazaki, K. Atmospheric-pressure plasma synthesis of carbon nanotubes. *J. Phys. D. Appl. Phys.* **44**, 174007 (2011).
6. Chen, B. et al. Ion chemistry in premixed rich methane flames. *Combust. Flame* **202**, 208–218 (2019).
7. Gershman, S. & Raitses, Y. Unstable behavior of anodic arc discharge for synthesis of nanomaterials. *J. Phys. D. Appl. Phys.* **49**, 345201 (2016).
8. Yang, G. & Heberlein, J. Instabilities in the anode region of atmospheric pressure arc plasmas. *Plasma Sources Sci. Technol.* **16**, 765–773 (2007).
9. Tachi, S., Tsujimoto, K. & Okudaira, S. Low-temperature reactive ion etching and microwave plasma etching of silicon. *Appl. Phys. Lett.* **52**, 616–618 (1988).
10. Coburn, J. W. & Winters, H. F. Plasma etching—a discussion of mechanisms. *J. Vac. Sci. Technol.* **16**, 391–403 (1979).
11. Liu, N. et al. Sensitive and single-shot OH and temperature measurements by femtosecond cavity-enhanced absorption spectroscopy. *Opt. Lett.* **47**, 3171–3174 (2022).
12. Haas, R. A. Plasma stability of electric discharges in molecular gases. *Phys. Rev. A* **8**, 1017–1043 (1973).
13. Ecker, G., Kröll, W. & Zöller, O. Thermal instability of the plasma column. *Phys. Fluids* **7**, 2001–2006 (1964).
14. Ju, Y. & Sun, W. Plasma assisted combustion: dynamics and chemistry. *Prog. Energy Combust. Sci.* **48**, 21–83 (2015).
15. Chung, H.-Y. et al. Synthesis of ultra-incompressible superhard rhenium diboride at ambient pressure. *Science* **316**, 436–439 (2007).
16. Fukuyama, H., Nakao, W., Susa, M. & Nagata, K. New synthetic method of forming aluminum oxynitride by plasma arc melting. *J. Am. Ceram. Soc.* **82**, 1381–1387 (1999).
17. Knight, R., Smith, R. W. & Apelian, D. Application of plasma arc melting technology to processing of reactive metals. *Int. Mater. Rev.* **36**, 221–252 (1991).
18. Pangilinan, L. E. et al. Enhanced hardening effects on molybdenum-doped WB_2 and WB_2–SiC/B_4C composites. *Chem. Mater.* **34**, 5461–5470 (2022).
19. Riley, J., Atallah, C., Siriwardane, R. & Stevens, R. Technoeconomic analysis for hydrogen and carbon co-production via catalytic pyrolysis of methane. *Int. J. Hydrogen Energy* **46**, 20338–20358 (2021).
20. Ananthanarasimhan, J., Lakshminarayana, R., Anand, M. S. & Dasappa, S. Influence of gas dynamics on arc dynamics and the discharge power of a rotating gliding arc. *Plasma Sources Sci. Technol.* **28**, 085012 (2019).
21. Go, D. B. & Venkattraman, A. Microscale gas breakdown: ion-enhanced field emission and the modified Paschen's curve. *J. Phys. D. Appl. Phys.* **47**, 503001 (2014).
22. Freton, P., Gonzalez, J. J. & Gleizes, A. Comparison between a two- and a three-dimensional arc plasma configuration. *J. Phys. D. Appl. Phys.* **33**, 2442–2452 (2000).
23. Haddad, G. N. & Farmer, A. J. D. Temperature determinations in a free-burning arc. I. Experimental techniques and results in argon. *J. Phys. D. Appl. Phys.* **17**, 1189–1196 (1984).
24. Namihira, T. et al. Temperature and nitric oxide generation in a pulsed arc discharge plasma. *Plasma Sci. Technol.* **9**, 747–751 (2007).
25. Staack, D., Farouk, B., Gutsol, A. F. & Fridman, A. A. Spectroscopic studies and rotational and vibrational temperature measurements of atmospheric pressure normal glow plasma discharges in air. *Plasma Sources Sci. Technol.* **15**, 818–827 (2006).
26. Liu, N. et al. Femtosecond ultraviolet laser absorption spectroscopy for simultaneous measurements of temperature and OH concentration. *Appl. Phys. Lett.* **120**, 201103 (2022).
27. Moon, S. Y., Choe, W. & Kang, B. K. A uniform glow discharge plasma source at atmospheric pressure. *Appl. Phys. Lett.* **84**, 188–190 (2004).
28. Eliasson, B. & Kogelschatz, U. Nonequilibrium volume plasma chemical processing. *IEEE Trans. Plasma Sci.* **19**, 1063–1077 (1991).
29. Wang, C. et al. A general method to synthesize and sinter bulk ceramics in seconds. *Science* **526**, 521–526 (2020).
30. Briant, C. L. The properties and uses of refractory metals and their alloys. *MRS Online Proc. Libr.* **322**, 305–314 (1994).
31. Teunissen, J. & Ebert, U. 3D PIC-MCC simulations of discharge inception around a sharp anode in nitrogen/oxygen mixtures. *Plasma Sources Sci. Technol.* **25**, 044005 (2016).
32. Belan, M. & Messanelli, F. Compared ionic wind measurements on multi-tip corona and DBD plasma actuators. *J. Electrostat.* **76**, 278–287 (2015).
33. Stoffels, E., Flikweert, A. J., Stoffels, W. W. & Kroesen, G. M. W. Plasma needle: a non-destructive atmospheric plasma source for fine surface treatment of (bio)materials. *Plasma Sources Sci. Technol.* **11**, 383–388 (2002).
34. Ombrello, T., Qin, X., Ju, Y. & Carter, C. Combustion enhancement via stabilized piecewise nonequilibrium gliding arc plasma discharge. *AIAA J.* **44**, 142–150 (2006).
35. Novoselov, A. G. et al. Turbulent nonpremixed cool flames: Experimental measurements, direct numerical simulation, and manifold-based combustion modeling. *Combust. Flame* **209**, 144–154 (2019).
36. Rousso, A. C. et al. Time and space resolved diagnostics for plasma thermal-chemical instability of fuel oxidation in nanosecond plasma discharges. *Plasma Sources Sci. Technol.* **29**, 105012 (2020).
37. Llewellyn-Jones, F. *Ionization and Breakdown in Gases* (Wiley, 1957).
38. Yugeswaran, S. & Selvarajan, V. Electron number density measurement on a DC argon plasma jet by stark broadening of Ar I spectral line. *Vacuum* **81**, 347–352 (2006).
39. Peacock, N. J., Robinson, D. C., Forrest, M. J., Wilcock, P. D. & Sannikov, V. V. Measurement of the electron temperature by Thomson scattering in Tokamak T3. *Nature* **224**, 488–490 (1969).
40. Modi, A., Koratkar, N., Lass, E., Wei, B. & Ajayan, P. M. Miniaturized gas ionization sensors using carbon nanotubes. *Nature* **424**, 171–174 (2003).

41. Delikonstantis, E., Scapinello, M., Van Geenhoven, O. & Stefanidis, G. D. Nanosecond pulsed discharge-driven non-oxidative methane coupling in a plate-to-plate electrode configuration plasma reactor. *Chem. Eng. J.* **380**, 122477 (2020).
42. Luong, D. X. et al. Gram-scale bottom-up flash graphene synthesis. *Nature* **577**, 647–651 (2020).
43. Deng, B. et al. Phase controlled synthesis of transition metal carbide nanocrystals by ultrafast flash Joule heating. *Nat. Commun.* **13**, 262 (2022).
44. Hong, Q.-J. & van de Walle, A. Prediction of the material with highest known melting point from *ab initio* molecular dynamics calculations. *Phys. Rev. B* **92**, 1–6 (2015).
45. Buinevich, V. S. et al. Fabrication of ultra-high-temperature nonstoichiometric hafnium carbonitride via combustion synthesis and spark plasma sintering. *Ceram. Int.* **46**, 16068–16073 (2020).
46. Buinevich, V. S. et al. Mechanochemical synthesis and spark plasma sintering of hafnium carbonitride ceramics. *Adv. Powder Technol.* **32**, 385–389 (2021).

Methods

Plasma generation set-up

The plasma generation set-up consisted of two carbon felt electrodes connected to graphite electrode bases. A piece of carbon felt was used to fabricate two disc electrodes of 25.4 mm in diameter. Two pieces of circular graphite blocks (99.9% purity, Amazon.com) with dimensions of 50 mm × 50 mm × 25 mm were fabricated with a computer numerical control machine to provide base supports for the carbon felt electrodes. The graphite electrode bases were then connected to the positive and negative tabs of a TDK-Lambda GENESYS+ programmable power supply system. The gap between the two electrodes was set at around 3 mm but can be adjusted for different applications. The full electrode set-up was housed in a glovebox filled with pure argon gas (Airgas, UHP300) at atmospheric pressure.

Temperature measurement

Rayleigh scattering. The temperature distribution in the plasma was measured in situ using Rayleigh scattering—a linear optical technique in which the signal is proportional to the total number density of molecules in the plasma, which can then be combined with the ideal gas law to infer the plasma temperature[34,35]. As a result, the Rayleigh scattering signal is inversely proportional to the plasma temperature. To conduct the measurement, an Nd:YAG laser (Quantel Q-Smart 850) was used to generate laser pulses with a wavelength of 532 nm, a pulse duration of 6 ns, a repetition rate of 10 Hz, a pulse energy of 34 mJ and a shot-to-shot variation of pulse energy within ±5%. The laser pulses were focused by a plano-convex lens with a focal length of 1 m into the central region of the plasma between the two carbon-tip electrodes. The Rayleigh scattering signals from the argon atoms along the laser line inside the plasma were imaged by an ICCD camera (Princeton Instruments PIMAX-4 1024i) with a gate time of 80 ns. The camera was equipped with a lens (Nikon AF-S Nikkor 50mm f/1.8) and a bandpass filter with a bandwidth of 1 nm centred at 532 nm to block interference from other wavelength ranges. The camera was synchronized with the laser using a delay generator (SRS DG645). Fifty shots of Rayleigh images were averaged to minimize the laser pulse shot-to-shot variation. Each temperature data point was obtained based on the 50 measurements. To determine the plasma temperature, the Rayleigh signals were calibrated using the reference Rayleigh signals at room temperature and atmospheric pressure (based on the inverse proportional relation between the Rayleigh signal and temperature, as mentioned above).

Grey-body radiation. We also measured the temperature of the plasma from the UV–Vis spectra captured with a custom-made system based on a Vision Research Phantom Miro M110 high-speed camera[47]. The camera recorded a heating video at a frame rate of 1,000 frames per second. The grey-body emissivity of the carbon materials was used and substituted into Planck's law, and the normalized spectral signals were acquired based on the parameters reported by the camera manufacturer. The result was further calibrated with a Newport Oriel 6700 Series Blackbody Infrared Light source. This measurement method is assumed to be reliable with a temperature range of 773–4,773 K, and the error is around ±100 K (ref. 48).

Heat diffusion simulation

We adopted a two-dimensional model to evaluate the temperature distribution from the plasma centre to the carbon tip, in which the temperatures of the plasma centre and the carbon felt were set at 7,000 K and 3,000 K, respectively. In the unit cell model, we assumed the width and height of the carbon tip as 10 μm and 50 μm, respectively. The distance between the two tip-enhanced carbon electrodes was 3 mm and the average distance between two carbon tips was 200 μm. The commercial COMSOL Multiphysics software, based on finite element analysis, was used to solve the steady-state heat diffusion equation.

E-FISH measurement

The electric field inside the plasma was measured in situ using E-FISH generation. Conceptually, E-FISH measures the electric field using the second harmonic signal of the excitation laser in the presence of an externally applied electric field. This second harmonic signal is quadratically proportional to the plasma electric field strength[36]. The set-up consisted of a Ti:sapphire laser (Coherent Astrella), which was used to generate laser pulses with a central wavelength of 800 nm, a bandwidth of 12 nm, a pulse duration of 80 fs at a repetition rate of 1 kHz and pulse energy of 152 μJ. This pulse energy was selected to improve the E-FISH signal-to-noise ratio and eliminate the second harmonic signal generated by the laser pulses themselves at the focal point. The laser pulses were focused by a plano-convex lens (f = 400 mm) into the central region of the plasma between the two electrodes housed in the argon-filled glovebox chamber. A long-pass filter was applied before the laser pulses entered the chamber to block any upstream second harmonic generation at 400 nm. Then, the E-FISH signal at 400 nm was generated from the 800-nm laser pulses in the electric field between the two carbon electrodes. The E-FISH signal was separated from the laser pulses by a dispersive prism and a dichroic mirror that transmits the light at 800 nm and reflects the light at 400 nm. The resulting clean E-FISH signal was collected by an ICCD camera (Princeton Instruments PIMAX-4 1024i) with a gate time of 60 ns. The camera was equipped with a lens (Nikon AF-S Nikkor 50mm f/1.8) and a bandpass filter (Edmund Optics 65-193) with a bandwidth of 10 nm centred at 400 nm to minimize the background noise. The camera was synchronized with the laser using a delay generator (SRS DG645). Each electric field data point was obtained based on 300 E-FISH measurements. The background noise (including plasma emissions) was recorded and subtracted from the E-FISH signal. To determine the final electric field, the E-FISH signals were calibrated by measuring the electric fields generated before breakdown with a d.c. power supply and corrected for the number density of molecules using Rayleigh scattering. The E-FISH measurements featured a spatial resolution of around 3 mm (estimated based on the confocal length of the laser beam) along the direction of propagation of the laser beam.

Numerical simulations for the time dynamics of the electron number density

A two-dimensional fluid simulation was conducted to illustrate the better uniformity and stability of USP compared with a conventional bare plate electrode plasma (Extended Data Fig. 4c). In the simulation, the discharge pressure is 1 atm and the initial temperature is 3,000 K. A set of time-dependent equations for species, gas temperature, electron energy and the external circuit was formulated[49,50] and then solved numerically. Argon plasma chemistry was also coupled to the equations. The chemical reaction mechanism consists of six species (Ar, Ar*, Ar_2, Ar^+, Ar^{2+} and electrons) and 19 reactions, including excitation, ionization, dissociation, recombination and quenching.

A volumetric plasma-heating channel using a pair of coaxial structured electrodes

A carbon felt rod is placed at the axial centre of a carbon felt tube to form a coaxial structure. The carbon felt rod serves as the cathode, whereas the carbon felt tube serves as the anode. Long fibres and short-fibre arrays are on the surfaces of both the carbon rod and tube, in which the long fibres from the two electrodes come into contact. A voltage was gradually applied from 0 V to about 33 V to generate the narrow gaps using Joule heat. The voltage was further elevated to around 42 V to initialize and stabilize the plasma.

Synthesis and sintering of the refractory alloys and ceramics

Synthesis of Hf(C,N). USP can reach temperatures of several thousand kelvins in less than 1 s, which could prevent nitrogen dissociation to successfully synthesize and sinter Hf(C,N). To investigate the synthesis of

Hf(C,N) by USP, we prepared a pellet from a mixture of HfC (99% purity) and HfN (99.5% purity) powders (Tongrun Info Technology), which were weighed with a nominal atomic ratio of Hf:C:N = 0.53:0.27:0.2, then mixed and ball-milled for 5 h. The tungsten carbide ball-milling jars were sealed with tape in an argon environment to protect the powders from oxidation during milling. The ball-milled powder was pressed into pellets with a diameter of 10 mm and placed on the surface of the lower electrodes in the gap between the two tip-enhanced carbon felt electrodes. A programmable power supply was used to generate the plasma and heat the pellets for 10 s at a plasma temperature of 4,400 K, 4,500 K, 4,800 K and 5,150 K, as measured by Rayleigh scattering. The sintered pellets were cooled down to room temperature for further characterization.

Synthesis of the W–1.5Nb–0.5Ti (wt%) refractory alloy. Tungsten (99.95% purity, 6K Additive), niobium (99.85% purity, Sigma-Aldrich) and titanium (99.98% purity, Sigma-Aldrich) powders were mixed with a nominal composition of 98 wt% W, 1.5 wt% Nb and 0.5 wt% Ti. The powder blend was further mixed with an Inversina 2L Tumbler Mixer (Inversina, Switzerland) for 5 h to reach a high homogeneity. The powder mixture was then printed into a 1 × 8 × 30 mm flat rectangular shape using the Binder Jetting method (ExOne Innvent+, Desktop Metal). A standard set of printing parameters for tungsten alloys was chosen for the printing process, including saturation at 60%, binder set time at 5 s, dry time at 10 s, layer thickness at 50 µm, roughing roller at 300 rpm and smoothing roller at 400 rpm. To minimize carbon contamination during the printing process, ExOne CleanFuse binder with low carbon content was used. After printing, the samples were cured in an oven at 200 °C for 8 h to develop strength for the following process of de-powdering and handling. After removing the excess powder with compressed air, the samples went through a debinding step of 30 min at 450 °C to decompose the binder into organic fumes that were evaporated, leaving the shaped powder mixture, which we then sintered using USP. The samples were placed on the surface of the lower electrode in the gap between the two carbon felt electrodes. The programmable power supply was used to generate plasma and heat the pellets for 10 s at a plasma temperature of about 4,700 K as measured by Rayleigh scattering. The samples were cooled down to room temperature for further characterization.

For comparison, one specimen with the same composition, 98W–1.5Nb–0.5Ti (wt%), was arc-melted and analysed (Extended Data Fig. 8b,c). The raw materials in pure metal form with a purity of greater than 99.99 wt% (W: 99.999 wt%, Nb: 99.999 wt% and Ti: 99.99 wt%; Alfa Aesar) were cleaned and weighed before placing them in the chamber of an arc-melter (ABJ-338, Materials Research Furnaces). The chamber was pumped and purged with pure argon until the chamber pressure reached 2 psi. The argon gas flashing process was repeated four times to ensure an inert environment inside the working chamber. The open-circuit voltage was at 85 V and the current was set at 350 A, which are the recommended maximum limits to avoid damage to the tungsten electrode. At the beginning of the arc-melting process, a high-purity Zr (>99.99 wt%; Alfa Aesar) piece was fully melted to further remove residual oxygen inside the chamber. Each melting lasted for about 1 min, followed by a 20-s furnace cooling with cold tap water running through the copper crucible. The melting process was repeated three times to enhance the homogeneity of the alloy composition. After melting, the samples were sliced and polished for microstructure analysis.

Synthesis of the CNTs. Carbon black powder (50 mg; MSE Supplies) was spread on the surface of the lower tip-enhanced electrode. The programmable power supply was used to generate the plasma and heat the samples for 10 s at a plasma temperature of around 6,600 K as measured by Rayleigh scattering. The material was cooled down to room temperature for further characterization (Extended Data Fig. 8d,e).

Synthesis of amorphous MgO. Most high-melting-point oxide materials are extremely difficult to transform into amorphous states using conventional techniques because of the simultaneous requirements of both high-temperature melting and rapid cooling. Amorphous phases of ultra-high-temperature oxides such as MgO are typically made by sputtering into thin films, but it is difficult to achieve bulk materials. To investigate the possibility of synthesizing amorphous MgO phase using USP, we pressed crystalline MgO powder (>99% purity, Sigma-Aldrich) into pellets with a diameter of 8 mm. After plasma initiation, the pellet sample was inserted into the gap between the two carbon felt electrodes and heated to about 6,000 K for 20 s until the pellet started to evaporate intensely. The plasma was turned off and the sample was quickly cooled down to room temperature in seconds by strong airflow.

Powder bed fusion–sintering process demonstration. The USP powder bed fusion–sintering set-up is shown in Extended Data Fig. 10a. A small cathode carbon felt electrode (with a diameter of 8 mm) was used for plasma generation, and the input current was carefully adjusted to focus the plasma beam into a filament with a column radius of approximately 1 mm. The anode electrode was replaced by a carbon felt strip, which served to support the sample pellet and facilitate electron transfer. The carbon felt strip was connected to a motor, enabling movement along a pre-programmed route (Extended Data Fig. 10b). Tungsten powders (99.9%, Atlantic Equipment Engineers) were pressed into a green pellet and put on the carbon felt strip. The plasma was turned on and the carbon felt strip carried the green pellet to move relative to the focused plasma. After scanning, the pellet sample was gradually cooled down to room temperature. The pellet was vertically mounted with epoxy resin, then ground and polished using different grades of sandpaper to expose its cross-section. The cross-sectional SEM image of the USP-processed tungsten pellet is shown in Extended Data Fig. 10c.

Coating deposition process. Boron (>98%, STREM Chemicals), molybdenum (99.9%, STREM Chemicals), tantalum (99.98%, STREM Chemicals), titanium (99%, STREM Chemicals), tungsten (99.95%, STREM Chemicals) and zirconium (99.5%, STREM Chemicals) powders were weighed at a ratio of $(Mo_{0.2}Ta_{0.2}Ti_{0.2}W_{0.2}Zr_{0.2})B_2$, mixed and ball-milled for 3 h. Boron powder 80 mol% excess was added to form the boron carbide phase and compensate for the evaporative loss of boron oxide during high entropy diboride (HEB) formation. The powder was further heated by a carbon heater in an argon-filled glovebox to 1,800 °C to trigger the self-propagating reactions. Toluene (45 wt%), fish oil (0.5 wt%) and the powders (40 wt%) were mixed and milled for 3 h. After that, polyvinyl butyral (6 wt%) and benzyl butyl phthalate (8.5 wt%) were added and milled for 6 h to form a slurry. The slurry was cast to form a coating on the surface of a Nb–10Hf–1Ti alloy substrate, followed by a calcination treatment at 450 °C for 1 h. A cathode carbon felt electrode (with a diameter of 25.4 mm) was used for plasma generation, and the anode electrode was the carbon felt strip to support the coating sample and facilitate electron transfer. The plasma was turned on and the carbon felt strip carried the HEB-coated alloy coupon to move and ensure that the sample could be evenly heated by the plasma. After scanning, the sample was gradually cooled down to room temperature. The cross-sectional SEM image of the coating on the substrate is shown in Extended Data Fig. 10d.

Materials characterization

The morphologies of the carbon felt electrodes and synthesized samples (CNTs, W–1.5Nb–0.5Ti, pure tungsten, HEB-coated Nb-10Hf-1Ti alloy, amorphous oxides and Hf(C,N)) were characterized using a Tescan XEIA SEM. The length and diameter measurements of the short carbon fibres were obtained from the measurements of 50 fibres using SEM. The average fibre density across the carbon felt electrode was measured across an area of 500 µm × 500 µm from five different SEM images for statistical results. XRD of the materials was measured

using a D8 Bruker Advanced X-ray Diffraction system using a Cu Kα radiation source operated at 40 kV and 40 mA. The scanning angles were from 10° to 80°. The Hf(C,N) samples were cryo-polished with an argon-ion beam cross-section polisher (JEOL, IB-19520ccp) with an observable cross-sectional area of about 900 μm × 600 μm. An Axia ChemiSEM (Thermo Fisher) was used for imaging (SEM) and elemental mapping using energy-dispersive spectroscopy of the cryo-polished cross-sections of these two samples. TEM imaging and electron energy-loss spectroscopy acquisition of the CNTs were carried out on a JEOL NEOARM system equipped with a Gatan 965 Quantum ER spectrometer at 200 kV.

Calculation of the Debye length

The Debye length (λ_D) describes the distance in which the charges are increasingly electrically screened and the electric potential decreases exponentially. It can be calculated using the following equation:

$$\lambda_D = \sqrt{\frac{k_B T_e \varepsilon}{n_e e^2}}$$

in which k_B is the Boltzmann's constant (1.38×10^{-23} J K^{-1} = 8.617×10^{-5} e V K^{-1}), T_e is the electron temperature (estimated to be 4,000–8,000 K in this work), n_e is the electron density (estimated to be 10^{-12} cm^{-3}), e is the electron charge, and ε is the plasma permittivity (55.26 e^2 eV^{-1} μm^{-1}). We assume T_e = 8,000 K and $n_e = 10^{12}$ cm^{-3}. Therefore, we can estimate λ_D to be about 6.2×10^{-6} m.

The average distance between the carbon fibres within the bundles in our tip-enhanced electrodes is about 1–10 μm, which is close to the Debye length calculated for our system. As a result, the tip-enhanced electric fields generated by the fibres can merge during the early stages of plasma formation, leading to a uniform, volumetric plasma.

Data availability

The data supporting the findings of this study are available in the paper and source data files. Further datasets collected for this study are available from the corresponding authors on request. Source data are provided with this paper.

47. Xie, H. et al. Ta–TiO_x nanoparticles as radical scavengers to improve the durability of Fe–N–C oxygen reduction catalysts. *Nat. Energy* **7**, 281–289 (2022).
48. Jacob, R. J., Kline, D. J. & Zachariah, M. R. High speed 2-dimensional temperature measurements of nanothermite composites: Probing thermal vs. gas generation effects. *J. Appl. Phys.* **123**, 115902 (2018).
49. Zhong, H., Mao, X., Mokrov, M. S., Shneider, M. N. & Ju, Y. 2D modeling of plasma dynamic contraction in the positive column of glow discharge. In *AIAA Sci. Technol. Forum Expo, AIAA SciTech Forum 2022* https://doi.org/10.2514/6.2022-1109 (AIAA, 2022).
50. Zhong, H., Shneider, M. N., Mokrov, M. S. & Ju, Y. Thermal-chemical instability of weakly ionized plasma in a reactive flow. *J. Phys. D. Appl. Phys.* **52**, 484001 (2019).

Acknowledgements This project was not directly funded. L.H. acknowledges support from the University of Maryland A. James Clark School of Engineering. Y.J. acknowledges the Department of Energy grant support for the Plasma Science Center and NSF EFRI. J.-C.Z. acknowledges the Minta Martin Professorship fund from the University of Maryland and the Clark Distinguished Chair Professor fund from the A. James & Alice B. Clark Foundation. J.L. and K.S. acknowledge partial support from the Air Force Office of Scientific Research (AFOSR) under grant no. FA9550-22-1-0413. S/TEM research was supported by the Center for Nanophase Materials Sciences (CNMS), which is a US Department of Energy, Office of Science User Facility at the Oak Ridge National Laboratory. We acknowledge the support from the University of Maryland NanoCenter and its AIMLab (Advanced Imaging and Microscopy Lab).

Author contributions L.H. and H.X. conceived the plasma concept. L.H., H.X., Q.Z. and S.L. carried out the plasma experimental studies, including materials syntheses. Y.J., H.X., N.L., M.N.S. and S.C. carried out the plasma instability analysis and characterization of the plasma, including Rayleigh thermometry and E-FISH measurements. J.-C.Z., J.L. and W.X. helped in planning the materials systems for the study, the shaped electrodes and sintering experiments and interpreting the results. H.X., D.L., K.S., J.L., Z.H, M.C., J.R., M.Z., X.W. and W.X. carried out the materials characterization. H.Z., X.Z. and A.D.L. conducted the plasma-related calculations. L.G. and Y.Y. conducted the cross-section polishing and SEM and EDX imaging of the MoNbTaW and Hf(C,N) samples. H.X., A.H.B., N.L. and L.H. wrote most of the paper. L.H., Y.J. and J.-C.Z. supervised the project. All authors contributed to the discussion and editing of the paper.

Competing interests L.H., H.X., Y.J., Q.Z. and J.-C.Z. report a patent application of 'Volumetric plasmas, and systems and methods for generation and use thereof' filed on 3 October 2022. A startup company, USPlasma Inc., was also established to help accelerate the application of USP.

Additional information

Supplementary information The online version contains supplementary material available at https://doi.org/10.1038/s41586-023-06694-1.

Correspondence and requests for materials should be addressed to Ji-Cheng Zhao, Yiguang Ju or Liangbing Hu.

Peer review information *Nature* thanks the anonymous reviewers for their contribution to the peer review of this work.

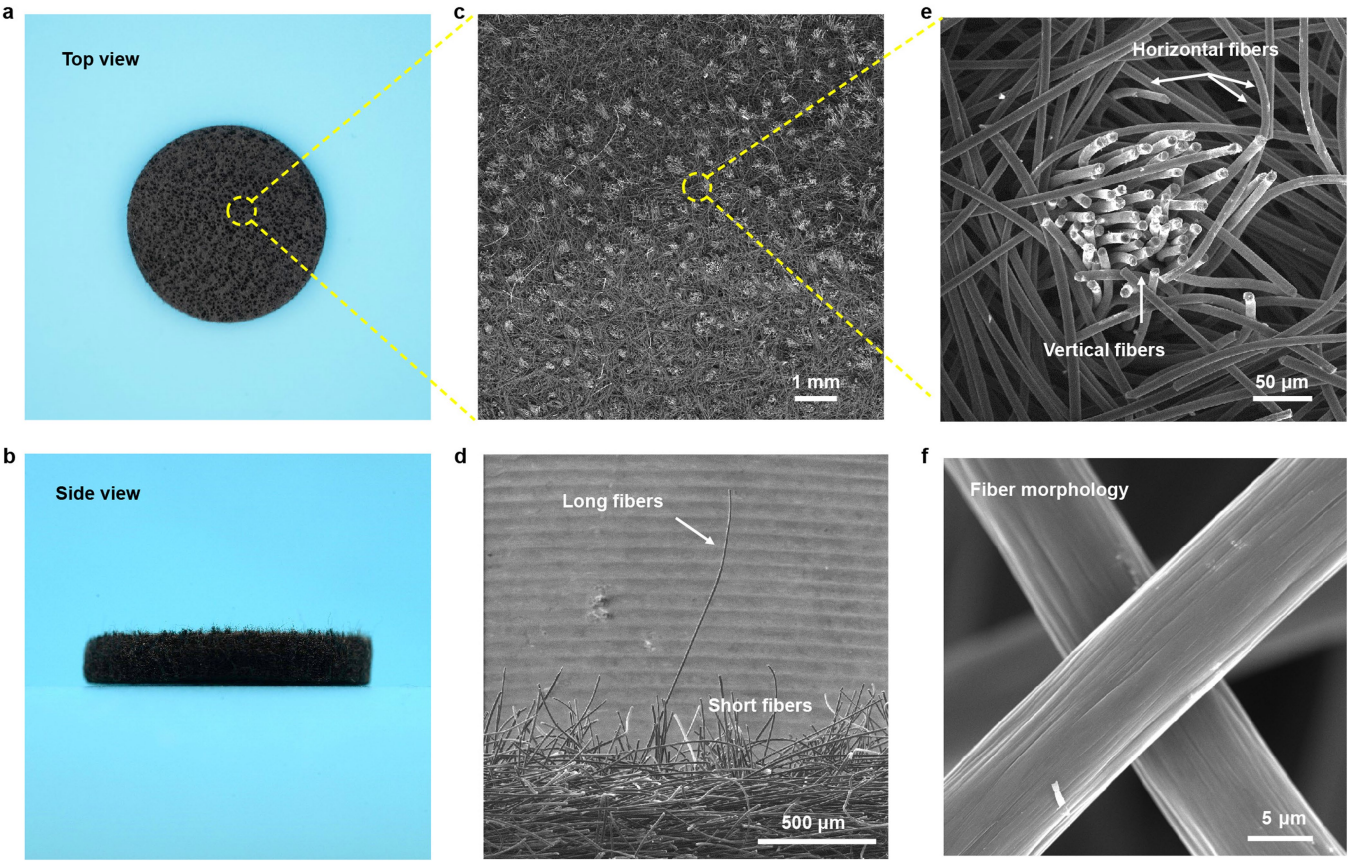

Extended Data Fig. 1 | The carbon felt electrode for USP. Fabrication of the carbon felt tip-enhanced electrodes. (a) Top view of a 25.4 mm diameter disk of carbon felt for the plasma electrodes. (b) Side view of the carbon felt electrode. (c) Top-view SEM image shows that the carbon felt electrode is composed of both horizontally (in-plane) and vertically-oriented (out-of-plane) carbon fibres. (d) Side-view SEM image of the carbon felt electrode showing the presence of both long and short vertically-oriented fibres. (e) Zoom-in SEM image of both the vertically-oriented short and horizontally-oriented long fibres with a vertically-oriented long fibre in the view as well. (f) Zoom-in SEM of the carbon fibres.

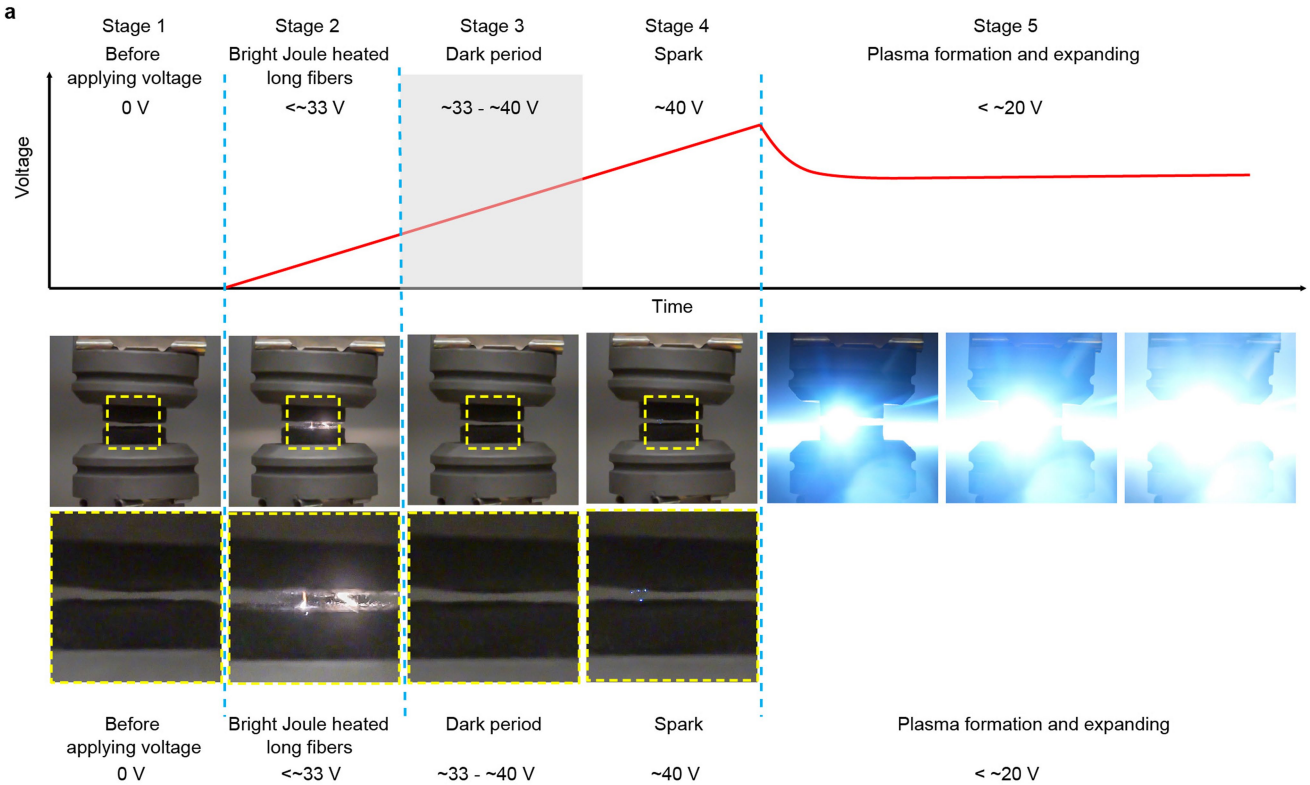

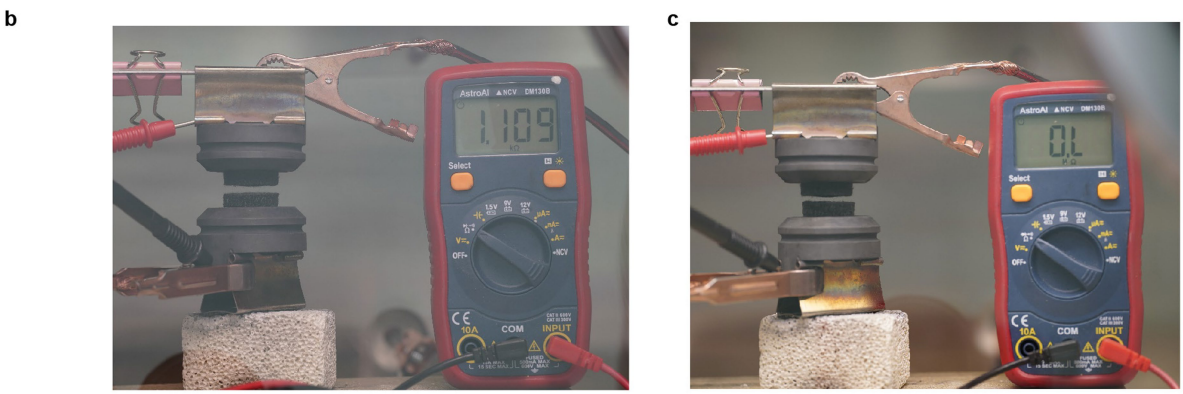

Extended Data Fig. 2 | USP formation by the carbon fiber electrodes. (a) Schematic of the voltage profile and corresponding photographs during the USP formation process. Before applying a voltage, the long carbon fibres come into contact across the two electrodes, with an observable resistance (1.109 kΩ) confirming the closed-circuit condition showing in (b). When applying a voltage, these long fibres generate Joule heat that ultimately deteriorates the points of contact where the resistance is highest. Eventually the fibres break, opening the circuit and resulting in a "dark" period of the plasma generation process in which no light or current signals are observed. At this stage, the resistance is infinite due to the breakage of the long fibres (c). The narrow gaps formed between the broken long fibres decrease the breakdown voltage (to ~42 V) by facilitating spark discharge via the field emission effect. Once the plasma is initialized, the densely spaced, vertically-oriented short carbon fibres of the electrode surfaces help rapidly expand the plasma to a large volume, which is accompanied by a voltage drop due to the increased conductivity of the plasma.

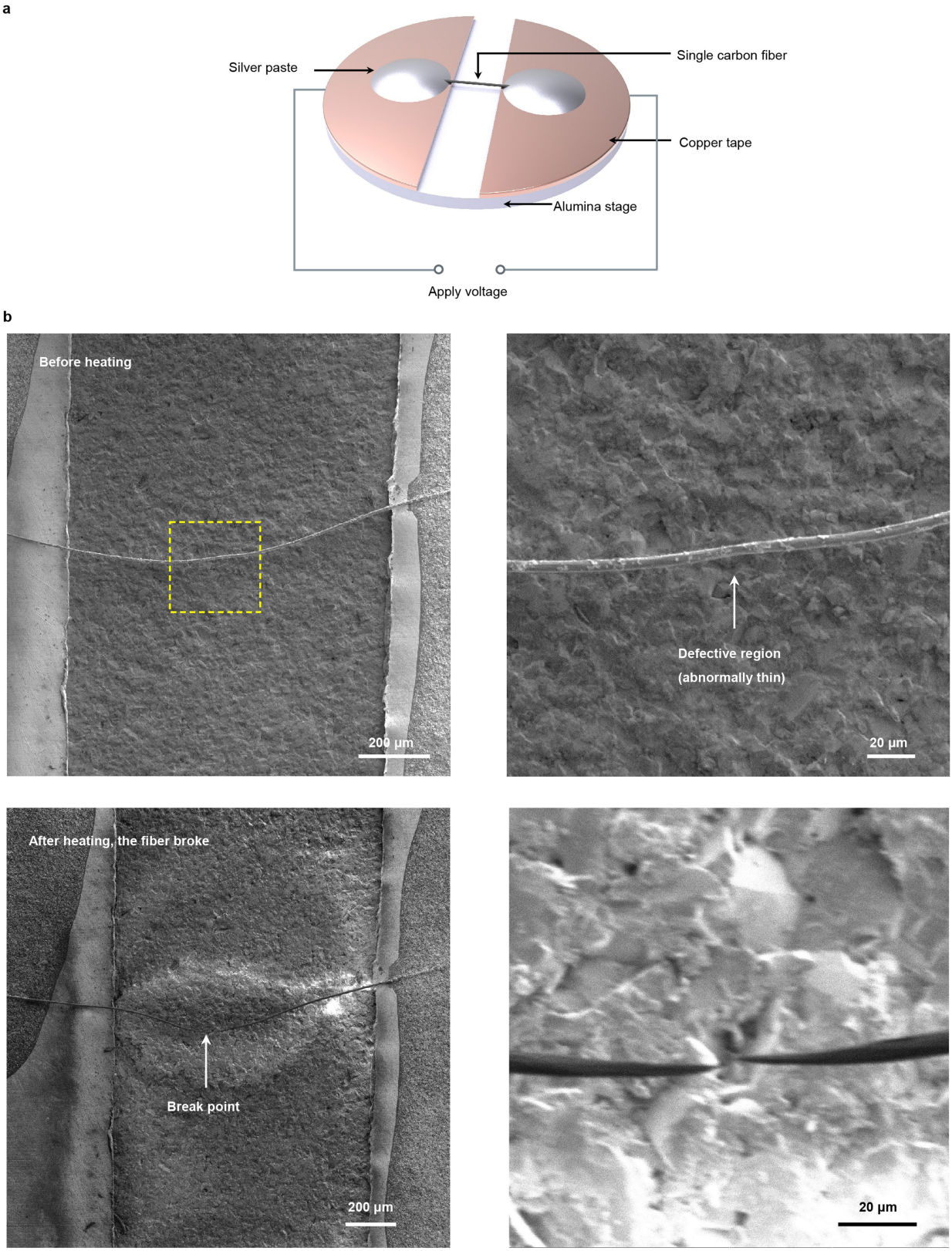

Extended Data Fig. 3 | In-situ SEM images showing the breakage of a single carbon fibre after Joule heating was applied. (a) The schematic shows the fibre heating setup for measurement of the resulting gap distance, in which a single carbon fibre is glued with silver paste onto a copper electrode stage and a voltage is applied to the fibre during SEM imaging. (b) SEM images of the fibre before Joule heating show a defective region in the fibre and SEM images of the fibre after Joule heating show that due to excessive heating, part of the carbon fibre is deteriorated, generating a small gap of ~3–5 μm—smaller than the diameter of the original fibre. The two edges of the fibre were also sharpened.

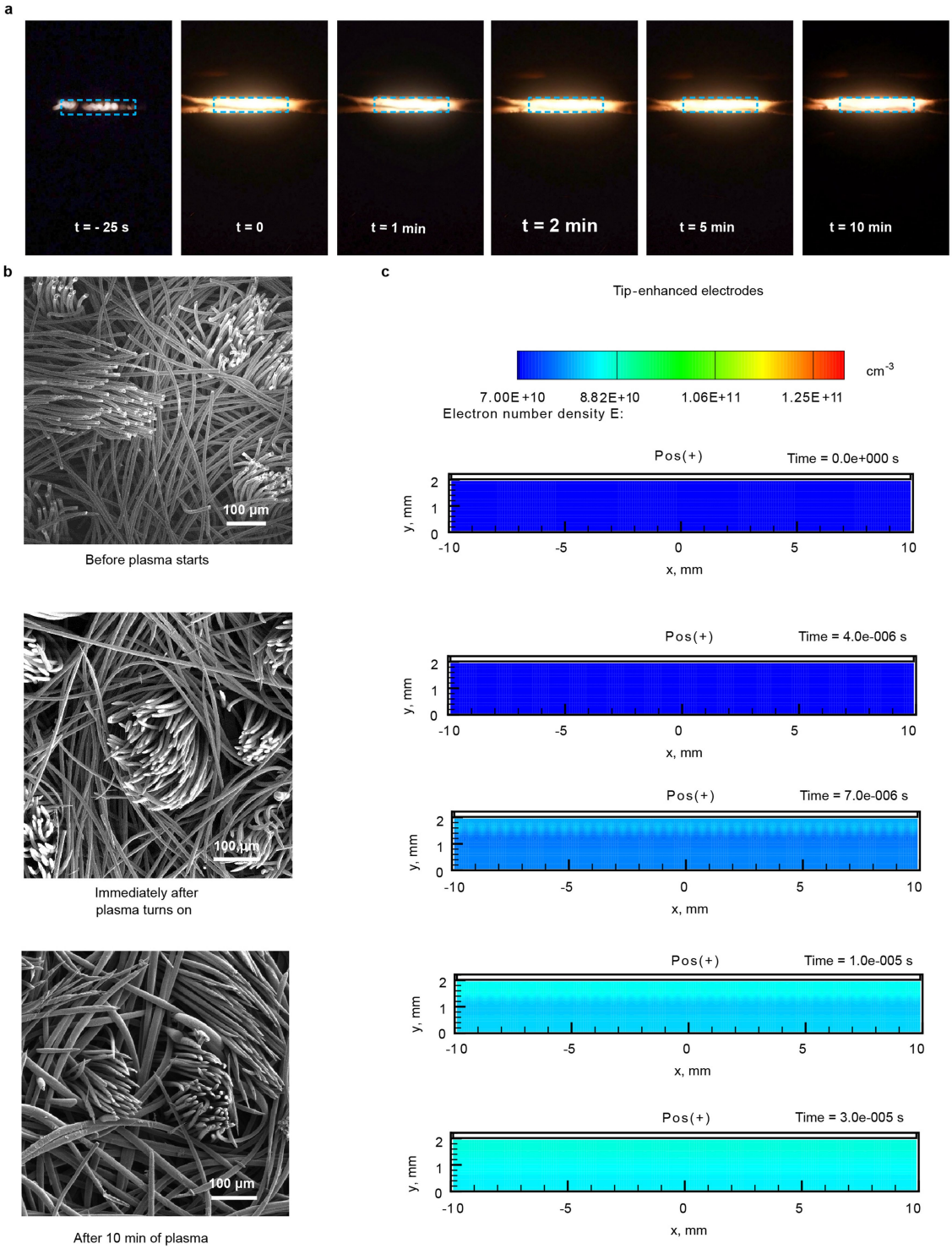

Extended Data Fig. 4 | The stability and uniformity of USP during 10 min operation. (a) The plasma was stable once initialized, running here for 10 min until we stopped the power supply. We set t = 0 when the gas discharge breakdown took place, and the plasma was on. The gap distance between the two electrodes was ~3 mm and the input current was 20 A. (b) SEM images demonstrating how the carbon fibre tip morphology changes before, immediately after the plasma initiation, and after 10 min of plasma operation. The vertical carbon fibres initially featured blunt tips and had sharper tips after the plasma generation, which were retained even after 10 min of plasma operation. (c) Numerical simulations demonstrating the evolution of the plasma over time. The scale bar indicates the electron number density. An initial thermal perturbation is set at the time point t = 0. The plasma usually tends to contract from a uniform and volumetric state, which is believed to be triggered by a change in the near-electrode plasma layers with time. Near the electrode surface, there are layers that release large amounts of heat, in which the thickness of the near-electrode layers is much smaller than the gap distance between the two electrodes. Here for simplicity, we treat the dynamics of the near-electrode layers as the initial temperature gradients near the electrode. The initial temperature gradients in the tip-enhanced electrode induced plasma are dispersed. The plasma density initially concentrates at the fibre tips, followed by homogenous expansion across the surface of the electrode to produce a uniform plasma.

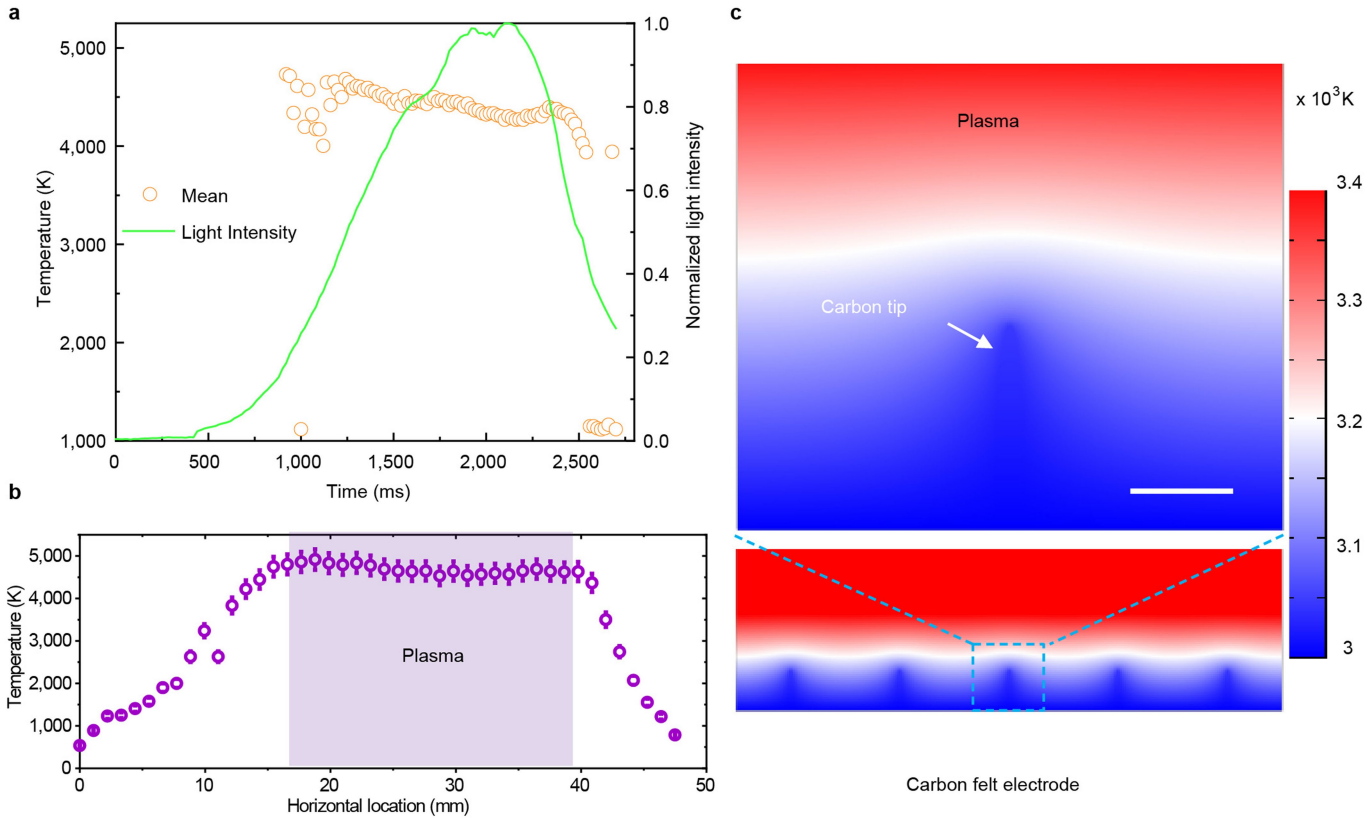

Extended Data Fig. 5 | The temperature profile of USP. (a) Measurement of the plasma temperature via the grey body radiation spectra when the current was 20 A (~4 A/cm^2). The plasma was initialized at ~1000 ms after the camera started to film. The power was then turned off from the electrodes at ~2500 ms. Upon initiation of the plasma, the temperature rapidly increases to ~4500 K. This measurement was consistent with the Rayleigh thermometry results. Note that the measurement accuracy of grey body radiation spectroscopy is ± 100 K. (b) Spatial temperature distribution of the plasma measured *in-situ* using Rayleigh scattering. A line scan showed the temperature was ~4700 K across the center of the plasma. The carbon tip array electrodes featured a diameter of 25.4 mm, with a gap of ~3 mm between the electrodes. The plasma was generated using a current of 20 A (4 A/cm^2). (c) The numerically simulated temperature distribution in the regions near the carbon fibre tips when the plasma is on. Numerical simulation shows the carbon tips featuring a lower temperature distribution, reaching just ~3000 K even when the plasma center is set at 7000 K. We attribute this to the high thermal conductivity and emissivity of the carbon tips, which helps rapidly transfer heat away from the electrodes. The scale bar is 20 µm.

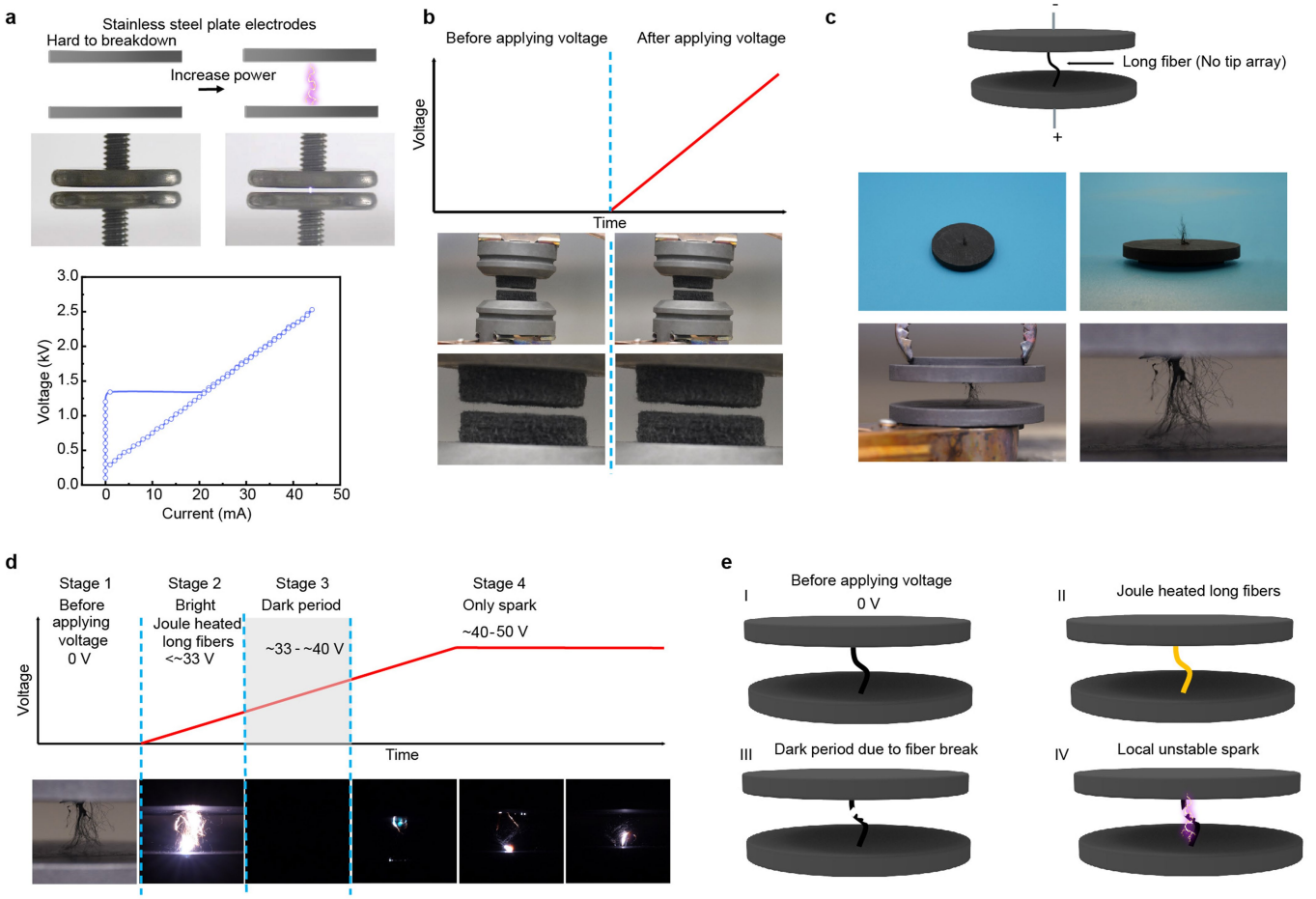

Extended Data Fig. 6 | Control experiments demonstrating the critical roles of the fibre tips. (a) Experimental setup of the stainless-steel plate electrodes (diameter = 25.4 mm), in which no carbon fibres were utilized. The corresponding current-voltage hysteresis loop indicates a gas discharge breakdown voltage of nearly 1,500 V over a ~3 mm gap was required, with the resulting plasma discharge occurring at random in narrow channels. (b) Carbon felt electrodes without long fibres. When there were no long fibre contacts, no spark discharge or plasma was formed. The voltage was increased from 0 to 80 V and no current was detected. (c) Schematic and photos of graphite plate electrodes with only a few long fibres connecting between them. We used 25.4 mm diameter graphite disks and glued a bundle of long carbon fibres to the center region, thus eliminating the effect of the short carbon fibres. The carbon fibre bundles were in contact with both the top and bottom graphite disks. (d) Control experiment for the plasma ignition without the short fibre tip array, in which the process used only long carbon fibres (as shown in (c)). The voltage was gradually elevated to 50 V, with corresponding photos of the electrodes shown. Obvious sparks can be seen in the photos as the voltage was increased to above ~40 V. However, due to the lack of short carbon fibres on the electrodes, the sparks did not lead to the formation of a continuous plasma and did not expand the plasma area across the graphite disk electrode. (e) Schematic showing the different stages for the electrodes with only long fibres when increasing the applied voltage. No continuous or stable plasma is formed.

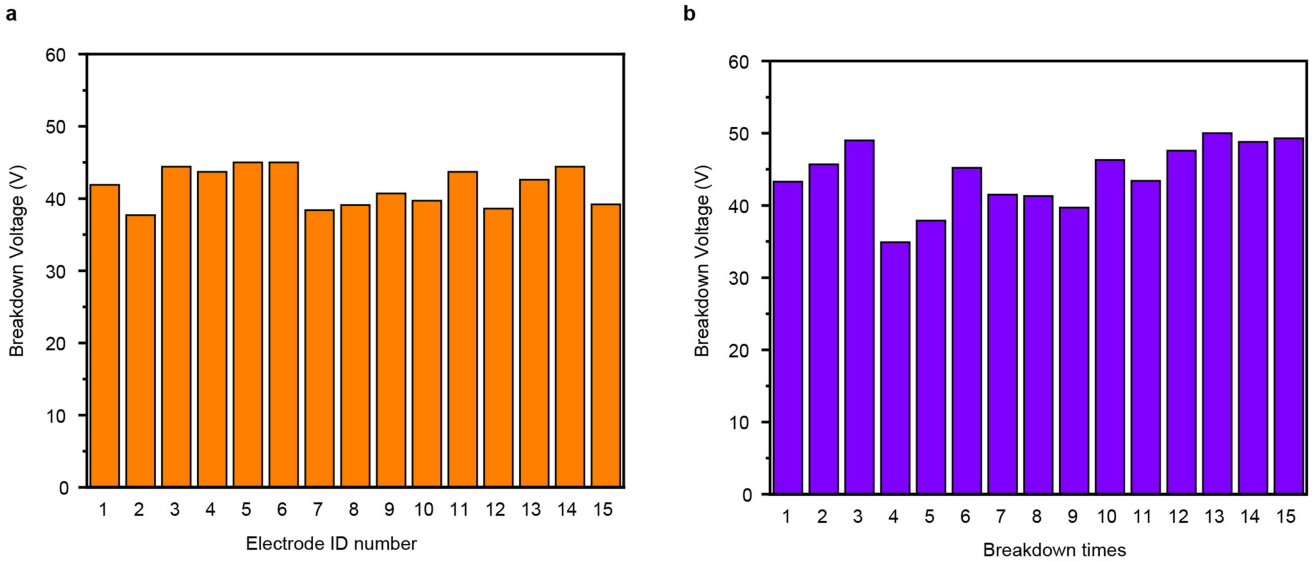

Extended Data Fig. 7 | Breakdown voltage measurements. (a) The breakdown voltage (41.6 ± 2.6 V, s.d.) for 15 pairs of the carbon fibre tip-enhanced electrodes. New electrodes were used for each measurement. (b) The breakdown voltage measurements, repeated 15 times, for the same pair of carbon fibre tip-electrodes with an average of 44.3 ± 4.4 V (s.d.).

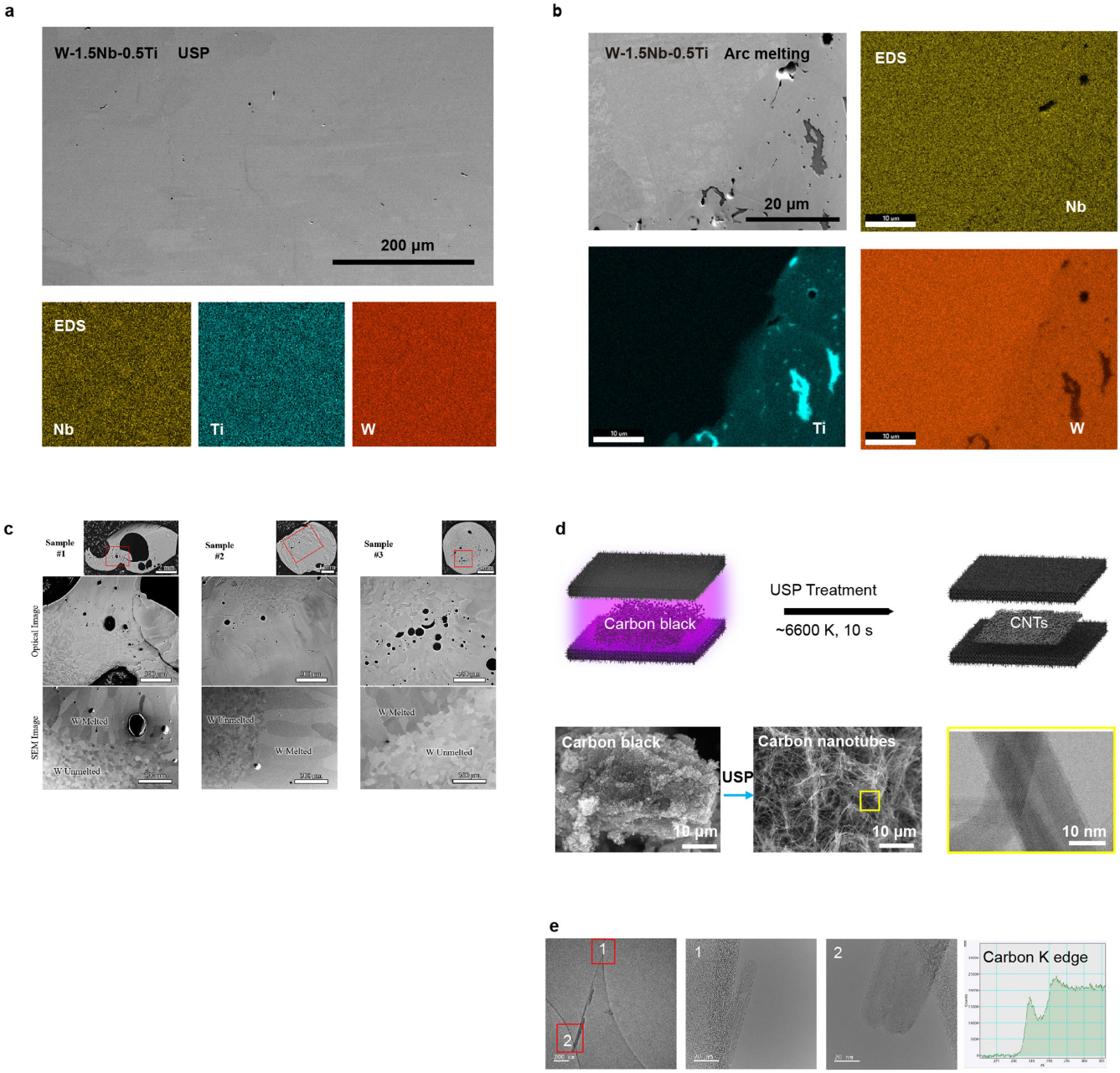

Extended Data Fig. 8 | The applications of USP for various materials synthesis. (a) SEM images and EDS mapping results of the W-1.5Nb-0.5Ti alloy cross section, in which the ultrahigh-temperature plasma (4700 K, ~10 s) readily melted the precursors to form a dense alloy with uniform distribution of the W, Nb, and Ti elements. (b) The W-1.5Nb-0.5Ti (wt%) sample made by arc melting. It is challenging to synthesize W-rich refractory alloys via arc melting since it is difficult for the tungsten cathode of the arc melter to generate a sufficiently high temperature to fully melt the tungsten. During arc-melting of this tungsten alloy, we observed pronounced heterogeneity in the microstructure, which indicated that the alloy elements were unable to melt uniformly, displaying notable segregation. It typically takes three to five times for arc melted samples to reach somewhat acceptable homogeneity. (c) Microstructural images of three W-1.5Nb-0.5Ti samples melted with different currents using a BJ-338 arc-melter from the Materials Research Furnace Inc. The starting materials were the elementary powders of W, Nb, and Ti. The currents were 280 A, 315 A, and 350 A for sample #1, sample #2, and sample #3, respectively. (d) Schematic and images demonstrating the direct synthesis of CNTs from carbon black via USP (~6600 K, ~10 s) without a catalyst. SEM and TEM images demonstrate the transition of carbon black to multiwalled CNTs composed of ~5–15 carbon layers after the USP treatment. (e) TEM image of a CNT and its ends. No metal nanoparticles were observed at the nanotube ends, confirming that no catalyst was involved in the synthesis. EELS analysis of the CNTs shows a typical carbon K edge profile. This approach could potentially improve the accessibility of CNTs, particularly by using low-cost carbon black (a byproduct of the petroleum industry) as a starting material.

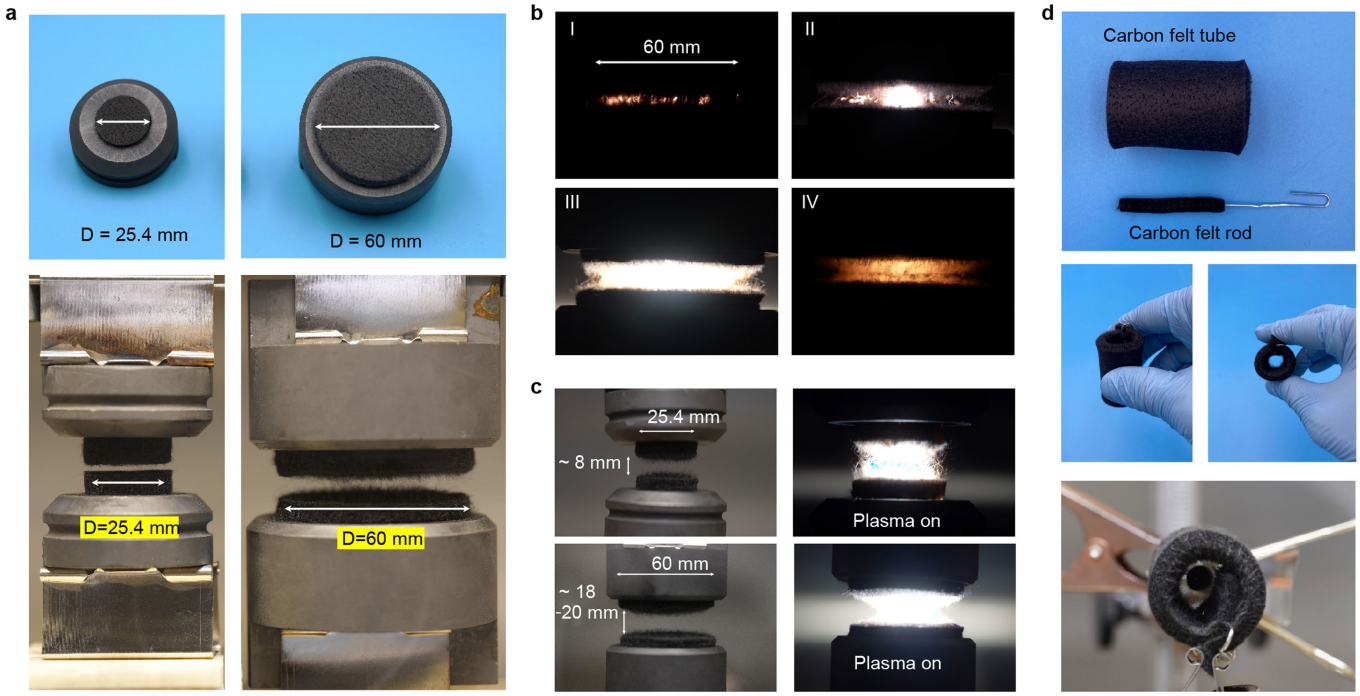

Extended Data Fig. 9 | The USP electrodes with different form factors. (a) Photos comparing the size of carbon felt electrodes with diameters of 25.4 mm and 60 mm, respectively. The area is enlarged by ~6-fold. (b) Ignition and stabilization of plasma between the 60 mm diameter electrodes. The gap distance between the two carbon felt electrodes was 10 mm. (c) The ignition and formation of plasma using electrodes with wider gap distances, including a 8 mm gap for the 25.4 mm diameter electrode, and a 18–20 mm gap for the 60 mm diameter electrode. (d) A coaxial carbon felt rod-tube structure to form a plasma-filled channel. The carbon felt rod serves as the cathode and the carbon felt tube is the anode. The metal hook is a current collector.

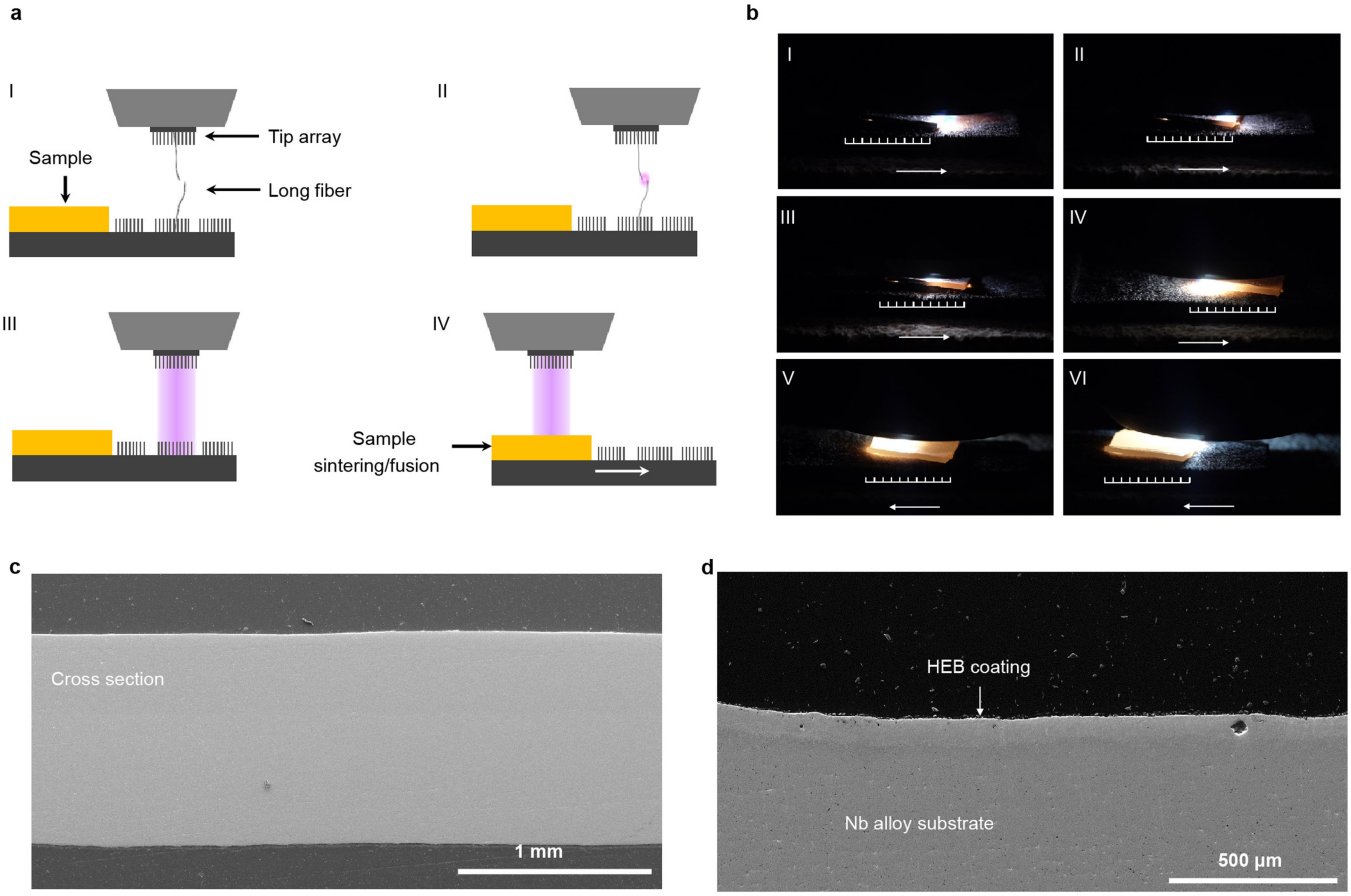

Extended Data Fig. 10 | The plasma sintering/fusion process using a focused plasma beam. (a) Schematic of the plasma sintering/fusion process. (I) The carbon felt electrodes are first placed directly across from each other. (II) The voltage is then elevated to realize the plasma breakdown. (III) With the aid of the short tip array, the plasma is spread and stabilized. (IV) The bottom carbon felt electrode then carries the sample to go under the plasma to realize sintering/fusion. (b) Photos showing the plasma fusion process. The pellet is carried by the carbon felt strip to scan the sample beneath the plasma heating region using a programmed route until the sample is well sintered. The scale bar shows the position of the sample. (c) Cross-sectional SEM image of a large tungsten sample achieved by the USP powder bed fusion/sintering process. (d) Cross-sectional SEM image of a high entropy diboride (HEB) coating on a Nb-10Hf-1Ti alloy substrate, in which good bonding was achieved without any gap between the coating and substrate.